Three-dimensional Green's tensor, local density of states, and spontaneous emission in finite two-dimensional photonic crystals composed of cylinders

D. P. Fussell,* R. C. McPhedran, and C. Martijn de Sterke
Center for Ultra-high Bandwidth Devices for Optical Systems & School of Physics, University of Sydney, Sydney, New South Wales 2006, Australia
(Received 7 November 2003; published 7 December 2004)

The three-dimensional local density of states (3D LDOS), which determines the radiation dynamics of a point-source, in particular the spontaneous emission rate, is presented here for finite two-dimensional photonic crystals composed of cylinders. The 3D LDOS is obtained from the 3D Green's tensor, which is calculated to high accuracy using a combination of a Fourier integral and the Rayleigh-multipole methods. A comprehensive investigation is made into the 3D LDOS of two basic types of PCs: a hexagonal cluster of air-voids in a dielectric background enclosed by an air-jacket in a fiberlike geometry, and a square cluster of dielectric cylinders in an air background. In the first of these, which has a complete in-plane band gap, the 3D LDOS can be suppressed by over an order of magnitude at the center of the air-voids and jumps sharply higher above the gap. In the second, which only has a TM gap in-plane, suppression is limited to a factor of 5 and occurs at the surface of the cylinders. The most striking band gap signature is the almost complete suppression of the radiation component of the 3D LDOS when the complete in-plane gap is sufficiently wide, accompanied by a burst into the radiation component above the gap.

DOI: 10.1103/PhysRevE.70.066608 PACS number(s): 42.70.Qs, 32.80.−t, 42.50.Dv

I. INTRODUCTION

Spontaneous emission may be regarded as one of the consequences of vacuum fluctuations, which Purcell [1] originally recognized were not immutable, but could be radically modified inside a cavity. Spontaneous emission can be both enhanced on-resonance [1] inside a cavity and suppressed off-resonance [2,3], relative to its rate in free-space. In fact, all that is required to modify spontaneous emission is for the density of photon states (DOS) to be altered, as has been demonstrated near a reflecting interface [4,5].

Originally proposed by Yablonovitch [6] and John [7], photonic crystals (PCs) are an area of rapidly growing interest, offering new possibilities for controlling the propagation of light [8]. Bragg scattering in the periodic dielectric structure of a PC can yield a photonic band gap (PBG) that prohibits propagation over a range of frequencies. The existence of the PBG is now well established by band structure calculations and the reconciliation of theory and experiment in reflection and transmission spectra [9]. A PC also dramatically rearranges the DOS about a PBG [6], transforming the emission characteristics of an embedded radiating source. The modified DOS can lead to inhibited spontaneous emission [6], the localization of photons [7], photon-atom bound states [10], and an anomalous Lamb shift [10–13]. A sharp band edge jump in the DOS also leads to novel non-Markovian effects that include fractionalized steady-state and oscillatory spontaneous emission [12,14–19], spectral splitting and subnatural linewidth [14], low threshold and rapid atomic switching [18,20], superradiance [15,21,22], and coherent phenomena [23–25].

Control of spontaneous emission has immediate application to improved efficiency in semiconductor devices like lasers, diodes, and solar cells [6], and possibly to new technologies like low-threshold lasers, ultrafast optical switches, all-optical transistors, and memory devices [18]. Despite these prospects, theory and experiment on spontaneous emission are far from being reconciled. Experiments on spontaneous emission have been conducted using luminescent dye impregnated in colloidal crystals [26–28] and opals [29–31], but the interpretation of the results has been impeded by a lack of applicable theory [31]. Furthermore, these experiments probe the DOS, which characterizes spontaneous emission averaged over a unit cell. PCs redistribute the DOS both in frequency and space, and the spatially resolved or local density of states (LDOS) [32,33] is the fundamental quantity that determines radiation dynamics. Non-Markovian effects were somewhat contentious as the isotropic and anisotropic band edge models adopted are not supported by the quadratic behavior for the DOS usually observed in 3D PCs [34]. However, recent accurate modeling of radiation dynamics using the LDOS in real absolute gap PCs has demonstrated the nonexponential decay phenomena predicted by these band edge models [19].

An experimental probe of the LDOS would require the measurement of radiation from a pointlike source (e.g., luminescent atom or molecule, quantum dot or dipolar antenna) at a particular location inside a finite-sized PC [35]. To-date, LDOS calculations have been limited to idealized PCs. The LDOS can be calculated for infinitely periodic two-dimensional (2D) and three-dimensional (3D) PCs using the Bloch method. This has been done for an array of cylinders [33], an array of spheres [33,34], and the cylindrical woodpile [36]. The LDOS has also been calculated for finite one-dimensional structures using multiple scattering theory [37] and the transfer matrix method [38]. Spontaneous emission rates in finite-sized PCs can be inferred from the classical dipole radiation power using the finite-difference time-

*Email address: fussell@physics.usyd.edu.au

domain (FDTD) method [39], by first assuming exponential decay. The main deficiency of this approach is computational inefficiency. The whole field across the structure is required to be evaluated for a single dipole orientation and typically only the emission rate for a few dipole orientations and positions is obtained. This has been done in 2D PCs composed of dielectric cylinders [40], the 2D slab structure [40,41], and the 3D inverted opal [42]. Large-scale investigations would be computationally prohibitive. Furthermore, the LDOS is the fundamental quantity that determines radiation dynamics and inferring the LDOS from the emission rate would need to be justified.

The preferred approach is to obtain the LDOS in a finite-sized PC via the Green's tensor. An accurate and efficient approach has been demonstrated for calculating the Green's tensor in finite stratified media [43]. The Green's tensor in more general finite-sized dielectric structures can be obtained by solving Dyson's equation [44]. Like the FDTD method, the structure is required to be discretized, limiting computational efficiency. Although this can be improved significantly by adapting the approach to the geometry of the medium, as has been done for a dielectric disk [45].

Recently, it was shown that a Rayleigh-multipole method can be used to calculate the Green's tensor accurately and efficiently in an arbitrary arrangement of aligned circular cylinders of infinite length [46]. This was used to calculate the 2D Green's tensor and the 2D LDOS, which apply to an infinite line-source, in a finite cluster of cylinders. It has since been shown that this approach can be extended to the 3D case for a point-source using a Fourier integral [35].

Although 3D PCs with complete 3D PBGs exhibit the strongest PBG effects, 2D PCs with complete 2D PBGs and partial 3D PBGs hold both substantial theoretical [8,47,48] and experimental [49,50] interest. They have taken many forms, including alumina cylinders in the microwave [49,51] and air-cylinders in glass [52], photonic crystal fiber [53], and 2D PC slab [54–56]. However, macroporous silicon [50], composed of a hexagonal array of cylindrical air-pores in a silicon background, remains the best example of an essentially ideal 2D PC system with a robust complete 2D PBG. This system is fabricated with an aspect ratio (pore height to pore diameter) of 100–500 and a pore separation leading to a PBG in the technologically important 1.5 μm wavelength range. While interest in 2D PCs is in part because of the relative ease of their fabrication, they also have numerous potential applications in their own right. These applications are usually based on 2D structures that contain defects [49,50] or a degree of stratification in the third dimension for confinement [54,57], and include basic optoelectronic components like waveguides [54,58,59] and resonant cavities [58,60], and more specific applications like fibers [53], lasers [61,62], and fiber lasers [63], among others.

This paper begins with a short description of the connection between radiation dynamics, in particular spontaneous emission, the LDOS, and Green's tensor in Sec. II. In Sec. III, the multipole method is detailed and extended to treat the more general geometry of a cluster of cylinders enclosed by a jacket. The computationally delicate treatment of a key Fourier integral is also addressed. In Sec. IV, the numerical implementation of this approach is validated by convergence testing. In Sec. V, the 3D LDOS is calculated as a function of both position and frequency and compared to the band structure. The sensitivities of the 3D LDOS to cylinder radius and refractive index contrast are also examined, along with the 3D-projected-LDOS (3D PLDOS). Finally, in Sec. VI, the results are summarized and their significance discussed.

II. SPONTANEOUS EMISSION, THE LDOS AND GREEN'S TENSOR

The radiation dynamics of a fluorescent source embedded in a host medium involves the source coupling to and interacting with the electromagnetic mode structure of the medium. The role of mode structure in radiation dynamics is completely embodied in a single quantity—the local density of states (LDOS) [15]. The focus here is on spontaneous emission, where a two-level atom decays from an excited state ($|a\rangle$) into a ground state ($|b\rangle$) by making an electric-dipole transition, and emitting a photon of energy $\hbar\omega_{ab}$ in the process. In 2D PCs, the LDOS is a sufficiently smooth function of frequency for the usual Weisskopf-Wigner theory of spontaneous emission [64] to apply. The decay is then exponential and the spontaneous emission rate is given in the electric-dipole approximation by Fermi's golden rule [65],

$$\Gamma(\mathbf{r}) = \frac{2\pi}{\hbar^2}\sum_f |\langle f|\hat{\boldsymbol{\mu}}\cdot\hat{\mathbf{E}}(\mathbf{r})|i\rangle|^2\delta(\omega_i-\omega_f), \tag{1}$$

where $|i\rangle$ and $|f\rangle$ are the initial and final state vectors of the atom-field system, and $\hat{\boldsymbol{\mu}}$ and $\hat{\mathbf{E}}(\mathbf{r})$ are the electric dipole and electric field operators, respectively. As shown by Sprik, van Tiggelen, and Lagendijk [32], the LDOS arises naturally upon splitting $\Gamma(\mathbf{r})$ into its atomic and field components,

$$\Gamma(\mathbf{r}) = \frac{\hbar\omega_{ab}}{2}\frac{2\pi|\langle a|\hat{\mu}|b\rangle|^2}{\epsilon_0\hbar^2}\rho(\mathbf{r},\omega,\hat{\mathbf{p}}), \tag{2}$$

where $\langle a|\hat{\mu}|b\rangle$ is the dipole transition moment and $\hat{\mathbf{p}}$ is the orientation of the dipole. In Eq. (2), $\rho(\mathbf{r},\omega,\hat{\mathbf{p}})$ is the LDOS for a particular dipole orientation, or projected-LDOS (PLDOS), and is defined as

$$\rho(\mathbf{r},\omega,\hat{\mathbf{p}}) = \sum_l |\hat{\mathbf{p}}\cdot\boldsymbol{\Psi}_l^E(\mathbf{r})|^2\delta(\omega-\omega_l). \tag{3}$$

The PLDOS is determined by the eigenfrequencies and eigenfunctions, ω_l and $\boldsymbol{\Psi}_l^E(\mathbf{r})$, of the Helmholtz equation in the host medium

$$\boldsymbol{\nabla}\times\boldsymbol{\nabla}\times\boldsymbol{\Psi}_l^E(\mathbf{r}) - \frac{\omega_l^2}{c^2}n(\mathbf{r})^2\boldsymbol{\Psi}_l^E(\mathbf{r}) = 0, \tag{4}$$

where $n(\mathbf{r})$ is the spatially dependent refractive index. The normalization condition applying to the eigenfunctions contains the weighting $\epsilon(\mathbf{r})$,

$$\int d^3\mathbf{r}\,\epsilon(\mathbf{r})\boldsymbol{\Psi}_l^{E*}(\mathbf{r})\cdot\boldsymbol{\Psi}_{l'}^E(\mathbf{r}) = \delta_{l,l'}. \tag{5}$$

The PLDOS is usually defined without this weighting (e.g., Ref. [33]) so that at positions in material it has a material

component in addition to the radiative component given by Eq. (3) [32]. However, it is the radiative component that appears explicitly in Eq. (2), and it is thus considered the more appropriate definition for determining spontaneous emission rates. The LDOS for a randomly oriented dipole source is obtained by averaging Eq. (2) over dipole orientation and absorbing the resulting 1/3 factor into the atomic part, giving

$$\rho(\mathbf{r},\omega) = \sum_l |\mathbf{\Psi}_l^E(\mathbf{r})|^2 \delta(\omega - \omega_l). \tag{6}$$

In a periodic structure, the usual DOS can be obtained by integrating Eq. (6) over a unit cell and using the normalization condition, Eq. (5), which gives

$$\rho(\omega) = \sum_l \delta(\omega - \omega_l). \tag{7}$$

The LDOS describes the local availability of modes to which a source can couple and emit a photon. It is clear from Eq. (6) that in general it varies with position. The DOS is still an important component in the LDOS, and in a complete band gap where the DOS is zero, the LDOS is also everywhere zero. However, the modes in a PC have nodes and antinodes separated by distances of the order of the wavelength of light [8]. This is typically three orders of magnitude greater than the size of an atom, so the LDOS and spontaneous emission rate can vary strongly with position when the DOS is nonzero. If modes have a preponderance of nodes at a certain position, then the LDOS can still be heavily suppressed. This is particularly relevant to the 2D PCs considered here, which have 3D pseudo gaps, but do not have 3D complete gaps. Spontaneous emission can also be enhanced when the DOS is enhanced, and Eq. (6) suggests that the enhancement is largest at locations where the relevant modes tend to have antinodes.

In periodic structures, the LDOS [Eq. (6)] can be evaluated directly by solving the eigenvalue problem (4) [33]. In finite structures, the preferred approach is via Green's function, or tensor [66,67]. The 3D Green's tensor describes the response of a medium to a point-source, as opposed to the 2D Green's tensor for an infinite line-source [68]. It is a powerful tool in electromagnetism (EM) that can be used in wave scattering from arbitrary source distributions [69], perturbation analysis [67], or simply to produce the emission pattern from a point-source. For a dipole point-source, the 3D LDOS is given by the trace of the electric Green's tensor ($\mathbf{G}^E$) [66],

$$\rho(\mathbf{r},\omega) = -\frac{2\omega}{\pi c^2}\mathrm{Im}\{\mathrm{Tr}[\mathbf{G}^E(\mathbf{r},\mathbf{r};\omega)]\}. \tag{8}$$

Note that the 3D LDOS is determined by the imaginary part of $\mathbf{G}^E$ at the location of the source. The 3D PLDOS is obtained after contracting $\mathbf{G}^E$ by $\hat{\mathbf{p}}$,

$$\rho(\mathbf{r},\omega,\hat{\mathbf{p}}) = -\frac{2\omega}{\pi c^2}\mathrm{Im}\{\hat{\mathbf{p}}^T \cdot [\mathbf{G}^E(\mathbf{r},\mathbf{r};\omega)] \cdot \hat{\mathbf{p}}\}. \tag{9}$$

It is easy to show that in a homogeneous medium with refractive index n, $\mathrm{Im}\{G^E_{0uu}(\mathbf{r},\mathbf{r})\} = -n\omega/6\pi c$; $\forall u \in \{x,y,z\}$. Using this in Eq. (8) then yields the familiar expression for the DOS in a homogeneous medium, $\rho(\omega) = n\omega^2/\pi^2 c^3 = n\rho_0(\omega)$ [70], where ρ_0 is the DOS in free-space.

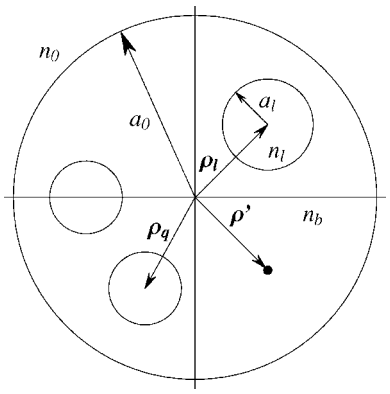

FIG. 1. The cross section of the scattering geometry composed of an arbitrary arrangement of cylinders with radius a_l and refractive index n_l, embedded in a background with refractive index n_b, and enclosed by a jacket with inner radius a_0 and refractive index n_0.

III. FORMALISM

The 3D LDOS in a 2D PC composed of a cluster of cylinders is obtained here from the 3D Green's tensor, which is calculated using a combination of a Fourier integral and a Rayleigh-multipole method. This involves a 3D full-vectorial treatment of EM wave scattering [69,71,72]. The 3D Green's tensor is a 3×3 matrix (or dyadic), $\mathbf{G}(\mathbf{r},\mathbf{r}')$, where the element $G_{uv}(\mathbf{r},\mathbf{r}')$ is the u coordinate of the field at $\mathbf{r}$ for a dipole point-source oriented in the direction of the v coordinate located at $\mathbf{r}'$. Both the electric, $\mathbf{G}^E$, and magnetic, $\mathbf{G}^H$, Green's tensors are evaluated in a piecewise homogeneous dielectric medium with refractive index $n(\mathbf{r}) = \sqrt{\epsilon(\mathbf{r})}$. This is done by solving the vector EM wave equations for a point-source in the form [69]

$$\nabla \times \nabla \times \mathbf{G}^E(\mathbf{r},\mathbf{r}') - k^2 n(\mathbf{r})^2\, \mathbf{G}^E(\mathbf{r},\mathbf{r}') = -\mathbf{I}\, \delta(\mathbf{r}-\mathbf{r}'),$$

$$\nabla \times \nabla \times \mathbf{G}^H(\mathbf{r},\mathbf{r}') - k^2 n\,(\mathbf{r})^2 \mathbf{G}^H(\mathbf{r},\mathbf{r}') = -\nabla \times \mathbf{I}\, \delta(\mathbf{r}-\mathbf{r}'), \tag{10}$$

where $k = 2\pi/\lambda = \omega/c$ is the vacuum wave number and $\mathbf{I}$ is the dyadic identity. Note that $\mathbf{G}^E$ and $\mathbf{G}^H$ are coupled by the boundary conditions, to be discussed in Sec. III B.

The general scattering geometry considered is a dipole point-source embedded in a finite cluster of N_c circular cylinders of infinite length, enclosed by a cylindrical jacket (Fig. 1). The radius of the lth cylinder is denoted by a_l, and its refractive index by n_l. The cylinders are embedded in a background of refractive index n_b, which is in turn enclosed by a jacket of infinite extent that has a refractive index of n_0, and an inner cylindrical boundary of radius a_0. The cluster is arranged in a cylindrical coordinate system, $(z,\boldsymbol{\rho}) = (z,\rho,\phi)$, with the cylinder axes aligned with the z-coordinate and the jacket centered on the origin. The point-source coordinates

are denoted $\mathbf{r}'=(z',\boldsymbol{\rho}')$ and the coordinate of the lth cylinder by $\boldsymbol{\rho}_l=(\rho_l,\phi_l)$. Cartesian coordinates, $\boldsymbol{\rho}=(x,y)$, are also used. The addition of a jacket allows for cylinders to be embedded in a background dielectric of finite extent ($n_b>1$ with $n_0=1$), extending the previous work in Ref. [35], which only allowed for a background of infinite extent. In summary, while this scattering geometry is 2D, the wave propagation from a point-source is 3D, leading to a 2.5D EM problem [69].

A. Homogeneous Green's tensor

The 3D Green's tensor in an infinite homogeneous medium, where $n(\mathbf{r})=n$ for all $\mathbf{r}$, is first examined to find an appropriate source-field expression. The homogeneous Green's tensor, $\mathbf{G}_n(\mathbf{r},\mathbf{r}')$, can be obtained from the scalar Green's function, g_n, using [69]

$$\mathbf{G}_n^E(\mathbf{r},\mathbf{r}')=\left[\mathbf{I}+\frac{\boldsymbol{\nabla}\boldsymbol{\nabla}}{(kn)^2}\right]g_n(\mathbf{r},\mathbf{r}'),$$

$$\mathbf{G}_n^H(\mathbf{r},\mathbf{r}')=\boldsymbol{\nabla}\times\mathbf{I}\,g_n(\mathbf{r},\mathbf{r}'), \tag{11}$$

where g_n is the solution to the Helmholtz equation,

$$[\boldsymbol{\nabla}^2+(kn)^2]\,g_n(\mathbf{r},\mathbf{r}')=\delta(\mathbf{r},\mathbf{r}'). \tag{12}$$

There are several different expressions for g_n that follow from adopting particular spectral decompositions of the source. The expression adopted here, using cylindrical coordinates, is [69]

$$g_n=-\frac{i}{8\pi}\int_{-\infty}^{\infty}d\beta e^{i\beta(z-z')}\,H_0^{(1)}(k_\rho|\boldsymbol{\rho}-\boldsymbol{\rho}'|), \tag{13}$$

where $H_0^{(1)}(z)$ is the zeroth order Hankel function of the first kind, $k_\rho=\sqrt{(kn)^2-\beta^2}$ is the in-plane component of the wave vector, and β is the propagation constant in the z-coordinate. Note that Eq. (13) is simply the inverse Fourier transform of

$$\tilde{g}_n=-\frac{i}{4}H_0^{(1)}(k_\rho|\boldsymbol{\rho}-\boldsymbol{\rho}'|), \tag{14}$$

and is the reason it is considered to be the most easily adapted source-field expression to the multipole approach below. The components of $\mathbf{G}_n$, obtained by using Eq. (13) in Eq. (11), are given in Appendix A.

B. Multipole method

The wave equations (10) in the configuration of Fig. 1 can be solved fully by exploiting the cylindrical geometry of the problem. A Fourier transformation in the z-coordinate is first made, giving wave equations for conical propagation. The z-components of the fields for a source oriented in the direction of the unit vector $\tilde{\mathbf{u}}$ are given by

$$(\boldsymbol{\nabla}_{\boldsymbol{\rho}}^2+k_\rho^2)\;\tilde{G}_{zu}^V(\boldsymbol{\rho},\boldsymbol{\rho}')=\mathcal{D}_u^V\;\delta(\boldsymbol{\rho}-\boldsymbol{\rho}'), \tag{15}$$

where $\tilde{\mathbf{G}}$ is the Fourier transform of the Green's tensor, $V\in\{E,H\}$, $k_\rho=\pm\sqrt{[kn(\mathbf{r})]^2-\beta^2}$, and

$$\mathcal{D}_u^E=\delta_{zu}+\frac{i\beta}{[kn(\mathbf{r})]^2}\,\boldsymbol{\nabla}\cdot\tilde{\mathbf{u}}\quad\text{and}\quad D_u^H=\tilde{\mathbf{z}}\cdot\boldsymbol{\nabla}\times\tilde{\mathbf{u}}$$

are differential operators. For in-plane propagation, $\beta=0$ and Eq. (15) reduces to the wave equations for the 2D Green's tensor addressed by Asatryan *et al.* [46]. The transverse components of the fields are straightforwardly obtained from the z-components using Maxwell's equations [69].

A multipole formulation is employed to solve Eq. (15) exactly. This is essentially an extension of the treatment of wave propagation in microstructured optical fibers by White *et al.* [73] to wave scattering from an embedded source. The reader is referred to Ref. [73] for more discussion on the important features of this method. The multipole method uses a field expansion in the vicinity of the lth cylinder in a Fourier-Bessel basis

$$V^l=\sum_{m=-\infty}^{\infty}[A_m^lJ_m(k_\rho\rho)+B_m^lH_m^{(1)}(k_\rho\rho)]e^{im\phi}, \tag{16}$$

where $J_m(z)$ is the Bessel function used to describe the convergent or source-free part of the field near $\rho=0$, and $H_m^{(1)}(z)$ is the Hankel function used for the divergent part. The local field expansion (16) only applies in the annulus from the lth cylinder surface to the nearest neighboring cylinder or source. The global field (or Wijngaard) expansion, which applies throughout the background, can be obtained using Green's second theorem,

$$\begin{aligned}\int_A&[V(\boldsymbol{\rho}'',\boldsymbol{\rho}')\boldsymbol{\nabla}_{\boldsymbol{\rho}''}^2\tilde{g}_b(\boldsymbol{\rho},\boldsymbol{\rho}'')-\tilde{g}_b(\boldsymbol{\rho},\boldsymbol{\rho}'')\boldsymbol{\nabla}_{\boldsymbol{\rho}''}^2V(\boldsymbol{\rho}'',\boldsymbol{\rho}')]\,dA_{\boldsymbol{\rho}''}\\&=\oint_{\partial A}\left[V(\boldsymbol{\rho}'',\boldsymbol{\rho}')\frac{\partial}{\partial n''}\tilde{g}_b(\boldsymbol{\rho},\boldsymbol{\rho}'')\right.\\&\quad\left.-\tilde{g}_b(\boldsymbol{\rho},\boldsymbol{\rho}'')\frac{\partial}{\partial n''}V(\boldsymbol{\rho}'',\boldsymbol{\rho}')\right]ds_{\boldsymbol{\rho}''},\end{aligned} \tag{17}$$

where A is the area of the background, ∂A is the boundary of this area, and n'' denotes the outward unit normal to ∂A at $\boldsymbol{\rho}''$. Upon evaluating Eq. (17) [46], the global expansion is given by

$$\begin{aligned}\tilde{G}_{zu}^{bV}(\boldsymbol{\rho},\boldsymbol{\rho}')=&-\frac{i}{4}\chi^b(\boldsymbol{\rho}')\mathcal{D}_u^V\{H_0^{(1)}(k_\rho|\boldsymbol{\rho}-\boldsymbol{\rho}'|)\}\\&+\sum_{l=1}^{N_c}\sum_{m=-\infty}^{\infty}B_{um}^{Vl}H_m^{(1)}(k_\rho|\boldsymbol{\rho}-\boldsymbol{\rho}_l|)e^{im\,\arg(\boldsymbol{\rho}-\boldsymbol{\rho}_l)}\\&+\sum_{m=-\infty}^{\infty}A_{um}^{V0}J_m(k_\rho\rho)e^{im\,\phi},\end{aligned} \tag{18}$$

where $\chi^b(\boldsymbol{\rho}')$ is a function, with value 1 in the background and 0 elsewhere, used to denote the presence of a point-source in the background. The first term on the right-hand side (RHS) of Eq. (18) gives the field from the point-source. The second term gives the field scattered from the cylinders, while the third gives that from the jacket. In the absence of scattering objects, only the point-source term remains, and Eq. (18) is simply the Fourier transform of $\mathbf{G}_{n_b}(\mathbf{r},\mathbf{r}')$.

The local [Eq. (16)] and global [Eq. (18)] field expansions are required to be consistent about each cylinder. This is enforced using Graf's addition theorem [74],

$$H_m^{(1)}(k_\rho|\boldsymbol{\rho}-\boldsymbol{\rho}_q|)e^{im\ \arg(\boldsymbol{\rho}-\boldsymbol{\rho}_q)} = \sum_{p=-\infty}^{\infty} H_{p-m}^{(1)}(k_\rho|\boldsymbol{\rho}_q-\boldsymbol{\rho}_l|)e^{i(m-p)\arg(\boldsymbol{\rho}_q-\boldsymbol{\rho}_l)} \times J_m(k_\rho|\boldsymbol{\rho}-\boldsymbol{\rho}_l|)e^{im\ \arg(\boldsymbol{\rho}-\boldsymbol{\rho}_l)}, \tag{19}$$

to transform the global expansion into the local coordinates of the lth cylinder. Equating Eqs. (16) and (18) then yields the Rayleigh identity,

$$A_{um}^{Vl} = K_{um}^{Vl} + \sum_{q=1,q\neq l}^{N_c}\sum_{p=-\infty}^{\infty} S_{mp}^{lq}B_{up}^{Vq} + \sum_{p=-\infty}^{\infty} S_{mp}^{l0}A_{up}^{V0}, \tag{20}$$

where

$$S_{mp}^{lq} = H_{m-p}^{(1)}(k_\rho\rho_q)e^{i(p-m)\phi_q},$$

and

$$S_{mp}^{l0} = (-1)^{m-p}J_{m-p}(k_\rho\rho_l)e^{i(p-m)\phi_l},$$

and K_{um}^{Vl} follow from the point-source term and are given in Appendix B. The Rayleigh identity (20) relates the converging field at each cylinder (LHS) to the diverging fields from all other source bodies (RHS) [73]. By the same approach, a second Rayleigh identity is obtained for the jacket,

$$B_{um}^{V0} = Q_{um}^{V0} + \sum_{q=1}^{N_c}\sum_{p=-\infty}^{\infty} S_{mp}^{0q}B_{up}^{Vq}, \tag{21}$$

where

$$S_{mp}^{0q} = J_{m-p}(k_\rho\rho_q)e^{i(p-m)\phi_q},$$

which relates the diverging field at the jacket to the diverging fields from the background sources. Introducing matrix notation where $\mathbf{A}_u^V=[\mathbf{A}_u^{Vl}]$ is a partitioned column vector composed of vectors of multipole coefficients, $\mathbf{A}_u^{Vl}=[A_{mu}^{Vl}]$, Eq. (20) then condenses to

$$\mathbf{A}_u^V = \mathbf{K}_u^V + \mathbf{S}\mathbf{B}_u^V + \mathbf{S}^{l0}\mathbf{A}_u^{V0}. \tag{22}$$

$\mathbf{K}_u^V$ and $\mathbf{B}_u^V$ are defined similarly to $\mathbf{A}_u^V$, while $\mathbf{A}_u^{V0}=[A_{mu}^{V0}]$. $\mathbf{S}=[\mathbf{S}^{lq}]$ is a block matrix composed of Toeplitz matrices, $[\mathbf{S}^{lq}]=[S_{mp}^{lq}]$, and $\mathbf{S}^{l0}$ is defined similarly. In this notation, Eq. (21) becomes

$$\mathbf{B}_u^{V0} = \mathbf{Q}_u^{V0} + \mathbf{S}^{0l}\mathbf{B}_u^V. \tag{23}$$

The field expansions inside a cylinder and in the jacket are obtained similarly to that in the background. With only the presence of the point-source in these two regions, the field expansions simplify greatly with no need for Rayleigh identities. The field expansion inside the lth cylinder is given by

$$\tilde{G}_{zu}^{lV}(\boldsymbol{\rho},\boldsymbol{\rho}') = -\frac{i}{4}\chi^l(\boldsymbol{\rho}')\mathcal{D}_u^V\{H_0^{(1)}(k_\rho|\boldsymbol{\rho}-\boldsymbol{\rho}'|)\} + \sum_{m=-\infty}^{\infty} C_{um}^{Vl}J_m(k_\rho\rho_l)e^{im\ \phi_l} = \sum_{m=-\infty}^{\infty}[Q_{um}^{Vl}H_m^{(1)}(k_\rho\rho_l) + C_{um}^{Vl}J_m(k_\rho\rho_l)]e^{im\ \phi_l}, \tag{24}$$

where the function $\chi^l(\boldsymbol{\rho}')$ indicates the presence of a point-source in the cylinder and Q_{um}^{Vl} is defined similarly to K_{um}^{Vl} in Appendix B. The field expansion in the jacket is given by

$$\tilde{G}_{zu}^{0V}(\boldsymbol{\rho},\boldsymbol{\rho}') = -\frac{i}{4}\chi^0(\boldsymbol{\rho}')\mathcal{D}_u^V\{H_0^{(1)}(k_\rho|\boldsymbol{\rho}-\boldsymbol{\rho}'|)\} + \sum_{m=-\infty}^{\infty} D_{um}^{V}H_m^{(1)}(k_\rho\rho)e^{im\ \phi} = \sum_{m=-\infty}^{\infty}[K_{um}^{V0}J_m(k_\rho\rho) + D_{um}^{V}H_m^{(1)}(k_\rho\rho)]e^{im\ \phi}. \tag{25}$$

The multipole coefficients are also constrained by the boundary conditions, which require the tangential components of the electric and magnetic fields to be continuous at the surfaces of the cylinders and jacket. For the cylinders, the boundary conditions yield the relation

$$\begin{bmatrix}\mathbf{B}^E\\ \mathbf{B}^H\end{bmatrix} = \begin{bmatrix}\mathbf{R}^{EE} & \mathbf{R}^{EH}\\ \mathbf{R}^{HE} & \mathbf{R}^{HH}\end{bmatrix}\begin{bmatrix}\mathbf{A}^E\\ \mathbf{A}^H\end{bmatrix} + \begin{bmatrix}\mathbf{T}^{EE} & \mathbf{T}^{EH}\\ \mathbf{T}^{HE} & \mathbf{T}^{HH}\end{bmatrix}\begin{bmatrix}\mathbf{Q}^E\\ \mathbf{Q}^H\end{bmatrix}, \tag{26}$$

or

$$\boldsymbol{\mathcal{B}} = \boldsymbol{\mathcal{R}}\boldsymbol{\mathcal{A}} + \boldsymbol{\mathcal{T}}\boldsymbol{\mathcal{Q}}, \tag{27}$$

where $\mathbf{R}^{EE}=\mathrm{diag}[R_m^{EE}]$ is a block diagonal matrix composed of the diagonal matrices $\mathbf{R}^{EEl}=\mathrm{diag}\{R_m^{EEl}\}$, and the other $\mathbf{R}$ matrices and the $\mathbf{T}$ matrices are defined similarly. In Eq. (27), $\boldsymbol{\mathcal{R}}$ and $\boldsymbol{\mathcal{T}}$ are the external reflection and transmission matrices, respectively, with their components given in Appendix C. For the jacket, the boundary conditions yield

$$\boldsymbol{\mathcal{A}}^0 = \boldsymbol{\mathcal{R}}^0\boldsymbol{\mathcal{B}}^0 + \boldsymbol{\mathcal{T}}^0\boldsymbol{\mathcal{K}}^0, \tag{28}$$

where $\boldsymbol{\mathcal{R}}^0$ and $\boldsymbol{\mathcal{T}}^0$ are the internal reflection and transmission matrices, respectively, also defined in Appendix C.

Using the matrix notation of Eq. (27), identity (22) becomes

$$\boldsymbol{\mathcal{A}}_u = \boldsymbol{\mathcal{K}}_u + \boldsymbol{\mathcal{S}}\boldsymbol{\mathcal{B}}_u + \boldsymbol{\mathcal{S}}^{l0}\boldsymbol{\mathcal{A}}_u^0, \tag{29}$$

where $\boldsymbol{\mathcal{S}}=\mathrm{diag}\{\mathbf{S},\mathbf{S}\}$. Similarly, identity (23) becomes

$$\boldsymbol{\mathcal{B}}_u^0 = \boldsymbol{\mathcal{K}}_u^0 + \boldsymbol{\mathcal{S}}^{0l}\boldsymbol{\mathcal{B}}_u. \tag{30}$$

Note that the boundary conditions couple the E and H fields, while they remain independent in the Rayleigh identities (29) and (30). Note also that the $\boldsymbol{\mathcal{R}}$ and $\boldsymbol{\mathcal{T}}$ matrices contain the material properties of the medium while the $\boldsymbol{\mathcal{S}}$ matrices con-

tain the underlying lattice structure. This separation of medium and lattice parameters is advantageous for perturbation theory [75].

The Rayleigh identities (29) and (30), and boundary conditions (27) and (28), combine to form a complete linear system. This system can be written as a single field identity,

$$[\mathcal{I} - \mathcal{R}(\mathcal{S} + \mathcal{S}^{0A}\mathcal{R}^{0}\mathcal{S}^{0B})]\mathcal{B} = \mathcal{R}[\mathcal{S}^{0A}(\mathcal{R}^{0}\mathcal{K}^{0} + \mathcal{T}^{0}\mathcal{Q}^{0}) + \mathcal{K}] + \mathcal{T}\mathcal{Q}. \quad (31)$$

The point-source terms are confined to the RHS and the eigenvalues of the medium can be obtained by setting the RHS to zero [73]. In the presence of a point-source, $\mathcal{B}$ is obtained with a single matrix inversion. The remaining multipole coefficients can then be obtained using the Rayleigh identities and boundary conditions.

C. Fourier integral

The full 3D Green's tensor is finally obtained by performing the inverse Fourier transformation,

$$\mathbf{G}^{E}(\mathbf{r},\mathbf{r}') = \frac{1}{2\pi}\int_{-\infty}^{\infty} d\beta\, e^{i\beta(z-z')}\, \tilde{\mathbf{G}}^{E}(\boldsymbol{\rho},\boldsymbol{\rho}'). \quad (32)$$

The integrand in Eq. (32) contains $k_\rho = \pm\sqrt{(kn)^2-\beta^2}$ terms, which for a lossless medium lead to branch point singularities in complex β-space on the Re$\{\beta\}$-axis at $\beta = \pm kn_i$, where $n_i = n_l, n_b, n_0$. For a medium with loss or gain these singularities shift off the axis. Depending on the geometry, the integrand also has poles on the Re$\{\beta\}$-axis in the range $k\,\min(n_l,n_b,n_0) < |\beta| < k\,\max(n_l,n_b,n_0)$, corresponding to bound modes, or near the axis, corresponding to leaky modes. The integration around these singularities is addressed by ensuring that the Sommerfeld radiation condition is satisfied, which is done on a contour above singularities for Re$\{\beta\} < 0$, and below for Re$\{\beta\} > 0$ [69].

For the numerical demonstrations in this section and the subsequent section, a small hexagonal cluster is used with $N_c = 7$ circular air-voids ($n_l = 1.0$) of radius $a_l/d = 0.45$ (where d is the lattice constant) in a silicon background of refractive index $n_b = 3.4$, enclosed by an air-jacket ($n_0 = 1.0$) of radius $a_0/d = 2.0$. This is a simple 2D PC with a fiberlike geometry that is most relevant to the important 3D LDOS results that follow. The focus will also be on the components of Im$\{\mathrm{Tr}[\mathbf{G}^{E}(\mathbf{r},\mathbf{r};\omega)]\}$ required in the calculation of the 3D LDOS [Eq. (8)].

The modes in the cluster are classified according to waveguide theory [76,77] and determine the behavior of the integrand. To demonstrate this, the integrand Im$\{\tilde{G}^{E}_{zz}(\boldsymbol{\rho},\boldsymbol{\rho})\}$ is shown in Fig. 2(a) for Re$\{\beta\} > 0$ on a radial contour just below the Re$\{\beta\}$-axis. The range $|\beta| < kn_l$ contains a continuous spectrum of radiation modes with k_ρ real in all regions. In this range the integrand is smooth and continuous. The range $kn_l < |\beta| < kn_b$ contains a discrete spectrum of bound modes with k_ρ real in the dielectric background and imaginary in the air-voids and air-jacket. The integrand contains singularities on the Re$\{\beta\}$-axis at these bound modes and varies sharply in their vicinity. For $|\beta| > kn_b$, there are no

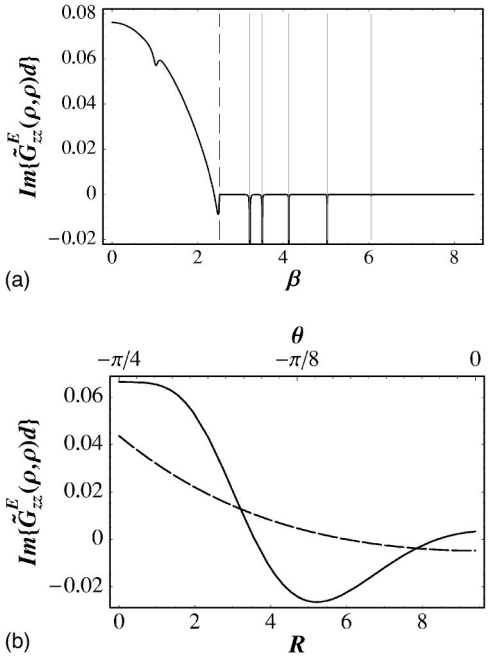

FIG. 2. Integrand of the Fourier inverse integral, Eq. (32). (a) Integrand on a radial contour with $\theta' = -10^{-5}$, along with the location of the bound modes (light-gray vertical lines). The vertical dashed line delineates radiation modes ($\beta < k$) from bound modes ($\beta > k$). (b) Integrand on Eq. (33) using $R' = 1.1kn_b$ and $\theta' = -\pi/4$, with the $\mathbb{C}_R$ part (solid line, top scale) and the $\mathbb{C}_\theta$ part (dashed line, bottom scale). The structure is a hexagonal cluster with parameters $N_c = 7$, $a_l/d = 0.45$, $n_l = 1.0$, $n_b = 3.4$, $a_0/d = 2.0$, and $n_0 = 1.0$. The frequency is $\omega d/2\pi c = 0.4$ and the position is $\boldsymbol{\rho} = (x,y)/d = (0.0, 0.0)$.

modes and Im$\{\tilde{G}^{E}_{uv}(\boldsymbol{\rho},\boldsymbol{\rho})\} = 0$ on the Re$\{\beta\}$-axis.

The Fourier integral is required to be performed numerically, but it would be computationally inefficient to do so close to the Re$\{\beta\}$-axis. By invoking the Cauchy integral theorem, the integrand can be evaluated along a contour off the Re$\{\beta\}$-axis that is appropriately confined to the second and fourth quadrants of the complex β-plane to comply with the Sommerfeld radiation condition. For Re$\{\beta\} > 0$, a convenient choice, after setting $\beta = Re^{i\theta}$, is a contour of the form

$$\mathbb{C} = \mathbb{C}_R \cup \mathbb{C}_\theta \cup \mathbb{C}_0 = \{\beta | 0 \leqslant R \leqslant R', \theta'\} \cup \{\beta | R', \theta' \leqslant \theta \leqslant 0\} \cup \{\beta | R' \leqslant R < \infty, 0\}, \quad (33)$$

composed of a radial component ($\mathbb{C}_R$) with $k\,\max(n_l,n_b,n_0) < R'$, an arc component ($\mathbb{C}_\theta$), and an axial component ($\mathbb{C}_0$), shown in Fig. 3. A similar contour above the axis is used for Re$\{\beta\} < 0$.

For calculating Im$\{\mathbf{G}^{E}(\mathbf{r},\mathbf{r})\}$, only the $\mathbb{C}_R \cup \mathbb{C}_\theta$ part of Eq. (33) is required. It is also easy to show that only the Re$\{\beta\} > 0$ part is needed for the diagonal components in

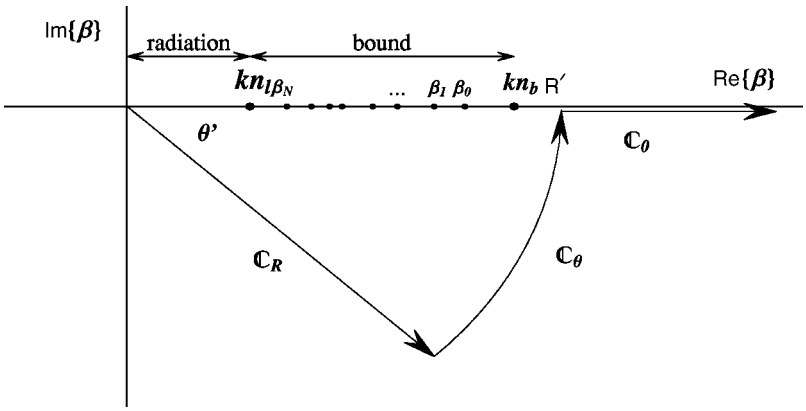

FIG. 3. The complex contour (33) for $\mathrm{Re}\{\beta\}>0$, with the branch point singularities at $\beta=kn_l, kn_b$ shown, along with the poles at the bound modes on the $\mathrm{Re}\{\beta\}$-axis.

$\mathrm{Im}\{\mathrm{Tr}[\mathbf{G}^E(\mathbf{r},\mathbf{r})]\}$, while both parts are required for the off-diagonal components of $\mathrm{Im}\{[\mathbf{G}^E(\mathbf{r},\mathbf{r})]\}$. The dramatic improvement in the behavior of the integrand on Eq. (33) using $\theta'=-\pi/4$ and $R'=1.1\times kn_b$ is shown in Fig. 2(b). These two contour parameters are generally found to optimize the convergence of the numerical evaluation of the Fourier integral. A contour of the form $\mathbb{C}_R\cup\mathbb{C}_\theta$ can also be used to isolate the radiation component by using $kn_l<R'<\beta_N$, where β_N is the propagation constant of the bound mode closest to kn_l (Fig. 3) .

IV. NUMERICAL VALIDATION

The field expansions, (18), (24), and (25), contain infinite sums derived from the local field expansion (16) and Graf's addition theorem (19). The numerical evaluation of the field expansions requires these to be truncated to $-N_m,\ldots,N_m$ so that each sum has in total $2N_m+1$ multipole terms. The convergence of $\mathbf{G}$ with respect to N_m is demonstrated in Fig. 4, where the relative difference, $\eta=|G_{N_m+1}-G_{N_m}|/|G_{N_m}|$, is plotted versus N_m. In general, the rate of convergence of a field expansion in Bessel functions becomes rapid in the large order limit where N_m significantly exceeds the argument in the Bessel functions. This is the regime of electrostatics where the largest order terms behave as $r^m\exp(im\theta)$ and $r^{-m}\exp(im\theta)$. Figure 4 shows that the rate of convergence is accordingly slightly more rapid at low frequencies, but depends primarily on the position in the cluster. For the structure modeled, the rate of convergence is most rapid at the center of cylinders in the low-index region where close to six figure accuracy is achieved with $N_m\approx 10$. Between two cylinders in the high-index region, the rate of convergence is slowest and limited to about four figure accuracy at $N_m\approx 18$. For $N_m\lesssim 20$, convergence is approximately exponential in accord with the electrostatic regime, while beyond this range machine precision begins to affect results and η begins to fluctuate wildly. Convergence is slower in structures with a higher refractive index contrast and larger cylinder radii, again because the argument in the Bessel functions is then larger.

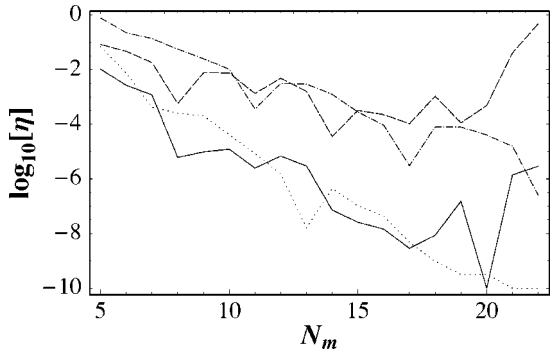

FIG. 4. The convergence of elements of the 3D Green's tensor with respect to the truncation parameter N_m. The relative difference $\eta=|G_{N_m+1}-G_{N_m}|/|G_{N_m}|$ is plotted for $\mathrm{Im}\{G_{zz}\}$ at $(x,y)/d=(0.0,0.0)$ for frequencies $\omega d/2\pi c=0.2$ (solid line) and 0.6 (dashed line), and for $\mathrm{Im}\{G_{xx}\}$ at $(x,y)/d=(0.5,0.0)$ for frequencies $\omega d/2\pi c=0.2$ (dotted line) and 0.6 (dash-dot line). The structure is the small hexagonal cluster used in Fig. 2.

The Fourier integral (32) is evaluated on the complex contour (33) using numerical quadrature. Simpson's rule is adopted and involves the abscissa of the integrand being decomposed into N_h intervals. The convergence of integration along both components of the contour with respect to N_h is demonstrated in Table I. In the low index region, the contribution of the $\mathbb{C}_\theta$ component is much smaller than the $\mathbb{C}_R$ component, while in the high index region, the contribution of both is similar. Accuracy better than four significant figures is assured for $N_h=16$ and six figures for $N_h=32$. This demonstrates that when the Fourier integral is evaluated on the complex contour, a high level of accuracy is achieved with relatively few abscissa points. This is important and leads to very high computational efficiency because almost all of the computation time goes into evaluating the multipole expansion at each abscissa point. Similar results are found for other coordinates, frequencies, and geometries where the essential behavior of the integrand shown in Fig. 2 is maintained. It is therefore adequate to use Simpson's rule with N_h fixed rather than more sophisticated adaptive routines. For a 3D LDOS calculation over a range of coordinates and frequencies in a given 2D PC, it is also adequate to use a fixed N_m. Clearly, N_m and N_h should be chosen so that the accuracy in the multipole sums and the quadrature are commensurate. Here, they are generally chosen to achieve 4–6 figure accuracy to ensure that at the very worst, the variation in convergence with position and frequency yields 2–4 figure

TABLE I. The convergence of the radial ($\mathbb{C}_R$) and ($\mathbb{C}_\theta$) contour components of $\mathrm{Im}\{G^E_{uv}(\mathbf{r},\mathbf{r})\}$ with respect to N_h at the frequency $\omega d/2\pi c=0.4$. The structure is the small hexagonal cluster used in Fig. 2.

N_h	$\mathrm{Im}\{G^E_{zz}[(0.0,0.0)/d,(0.0,0.0)/d]\}$		$\mathrm{Im}\{G^E_{xx}[(0.0,0.5)/d,(0.0,0.5)/d]\}$	
	$\mathbb{C}_R$	$\mathbb{C}_\theta$	$\mathbb{C}_R$	$\mathbb{C}_\theta$
6	0.100 252 172	0.007 499 401	−0.459 822 761	0.911 654 546
8	0.098 555 853	0.007 499 095	−0.459 814 136	0.912 114 488
12	0.098 769 214	0.007 498 962	−0.459 815 784	0.912 363 219
16	0.098 773 924	0.007 498 937	−0.459 815 908	0.912 401 820
24	0.098 788 139	0.007 498 927	−0.459 815 911	0.912 409 352
32	0.098 787 173	0.007 498 925	−0.459 815 913	0.912 409 606
48	0.098 786 956	0.007 498 924	−0.459 815 914	0.912 409 621

accuracy. The results in Sec. V A were obtained using $N_m=14$ and $N_h=16$, and the results in Sec. V B were obtained using $N_m=5$ and $N_h=16$.

V. LOCAL DENSITY OF STATES (LDOS)

A. Hexagonal cluster of cylindrical air-voids in dielectric (PC1)

1. Band structure

As is clear from Eq. (6), the LDOS in a periodic structure is determined by its band structure and modal field patterns. Even though the structures considered here are finite, they are sufficiently large for there to be a strong correspondence between the LDOS and band structure, and comparing the two is useful for understanding the LDOS results. For the 3D LDOS in 2D PCs, both the in-plane and out-of-plane band structures are relevant. These essentially characterize the DOS, and to a significant extent the LDOS as a function of frequency. An understanding of the modal field patterns would provide insight into the spatial variation of the 3D LDOS, but is beyond the scope of this paper.

The first general structure examined is a hexagonal cluster of cylindrical air-voids in a dielectric background (PC1). The main emphasis is on macroporous silicon [50] with a silicon background of refractive index $n_b=3.4$. The focus will be on an air-void radius of $a_l/d=0.45$, which was found to produce the most interesting results. Macroporous silicon can, however, be fabricated with a broad range of values for the air-void radius, and other values will be considered, along with other values for the background refractive index. The in-plane band structure for the underlying lattice is shown in Fig. 5. TE gaps are favored in this type of 2D PC [8], and it has a wide TE-gap in the frequency (normalized) range $\omega d/2\pi c=0.303-0.495$ ($\Delta\omega/\omega_0=48.0\%$). There is also a narrower TM gap in the frequency range $\omega d/2\pi c=0.405-0.445$ ($\Delta\omega/\omega_0=9.4\%$), which lies wholly within the TE gap to form a complete in-plane gap.

The in-plane component of the wave vector is given by

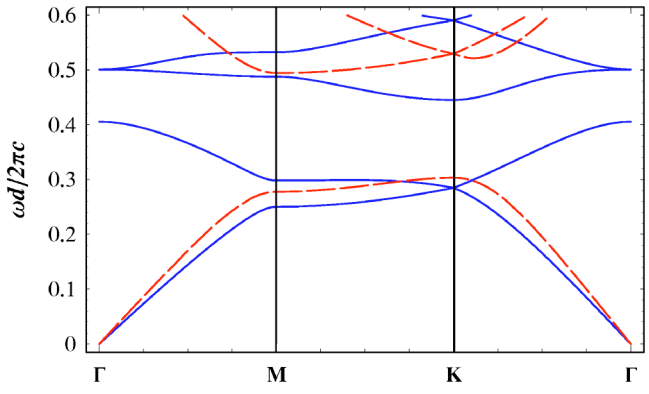

FIG. 5. 2D band structure for a hexagonal (or triangular) array of air-voids in a dielectric (PC1). The array parameters are $a_l/d=0.45$, $n_l=1.0$, and $n_b=3.4$ (i.e., macroporous silicon). The TM modes are shown as solid lines and the TE modes are shown as dashed lines.

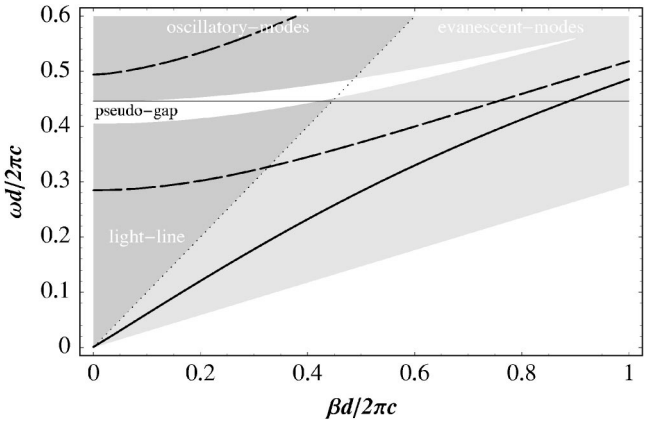

FIG. 6. Out-of-plane band structure for PC1 (see Fig. 5). The dark-gray region to the left of the light-line in air ($\omega=\beta$) indicates oscillatory modes with k_ρ real in air, while the light-gray region between the light-line in air and the light-line in the dielectric ($\omega=\beta/n_b$) indicates evanescent modes with k_ρ imaginary in air. The pseudogap indicates the (ω,β)-region where there are no modes. The horizontal line indicates the frequency where the pseudogap covers the largest range of β-values. The dashed lines indicate the bands emanating from the in-plane TE gap. The bold upward sloping line indicates the band emanating from the in-plane TM Γ-point.

$$k_\rho = \sqrt{n^2 \frac{\omega^2}{c^2} - \beta^2}, \tag{34}$$

where β is the propagation constant, so that for in-plane propagation $\beta=0$, and for out-of-plane propagation $\beta>0$. The out-of-plane band structure for macroporous silicon is shown in Fig. 6. For clarity, only the out-of-plane band segments emanating from the edges of the in-plane TE and TM band gaps are shown. The segment from the Γ-mode on the first TM band is also shown and is indicative of the β of the fundamental mode at each ω. As the propagation angle increases out-of-plane, indicated by increasing β in the figure, the bands shift to higher frequencies. When β is small near the in-plane band gaps, multiple scattering effects remain important and the band structure for a given β-value is mostly determined by the in-plane band structure at the projected frequency, indicated by k_ρ. The in-plane band structure effectively anchors k_ρ, and Eq. (34) with k_ρ fixed is a rough guide to dispersion in the β-direction. As a result, the out-of-plane bands slope upward with low dispersion in the β-direction when β is small, and get steeper as β increases. When β is large, index-guiding takes over with $\omega \sim \beta/n_b$, and the out-of-plane bands are correspondingly near parallel to the light-line in the dielectric background.

For 3D wave propagation in a 2D PC, it is not possible to have a complete band gap that covers all propagation directions. However, as shown in Fig. 6, a pseudogap, or a $(\omega-\beta)$-region where there are no modes, emanates from the complete in-plane gap. There is also a large $(\omega-\beta)$-region in the figure that emanates from the TE gap where there is a dearth of modes. Along with the out-of-plane bands, the pseudo gap is upward sloping in the $(\omega-\beta)$-diagram. As a result, the pseudogap covers the widest range of β-values just below the top of the complete in-plane gap. The out-of-plane diagram is also delineated by the light-line $(\omega=\beta)$ into modes that are oscillatory in air $(\omega>\beta)$ and modes that are evanescent in air $(\omega<\beta)$. As frequency increases inside the complete in-plane gap, the pseudogap covers a widening range of oscillatory modes. If the complete in-plane gap is sufficiently wide, the pseudogap may cover all oscillatory modes near the top of the in-plane gap. At the top of the complete in-plane gap, the first mode encountered is a radiation mode with $\beta=0$. Above the in-plane gap, the pseudogap rapidly goes from covering oscillatory modes to covering a narrowing range of evanescent modes.

2. Local density of states

The 3D LDOS in macroporous silicon was originally examined for a cluster of air-voids in an infinite silicon background [35] (i.e., without an air-jacket). In Fig. 7, the 3D LDOS is shown across the plane of a macroporous silicon cluster enclosed by an air-jacket. The cluster is composed of $N_c=37$ hexagonally packed air-voids with an air-jacket of radius $a_0/d=4.0$. The frequency $(\omega d/2\pi c=0.445)$ is just below the top of the complete in-plane gap (see Fig. 6). Enclosing the cluster by a jacket appears to have little impact on the spatial distribution of the 3D LDOS inside the cluster. As for an infinite silicon background [35], the 3D LDOS is

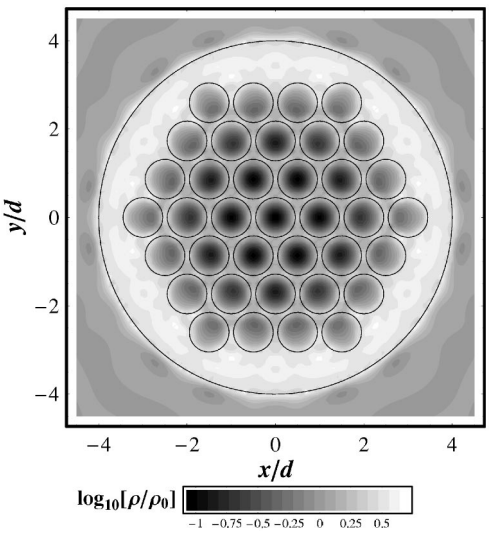

FIG. 7. 3D LDOS across the plane of a macroporous silicon cluster enclosed by an air-jacket. The frequency is $\omega d/2\pi c=0.445$ and the cluster parameters are $N_c=37$, $a_l/d=0.45$, $n_l=1.0$, $n_b=3.4$, and $a_0/d=4.0$. The 3D LDOS is normalized to its free-space value, $\rho_0=\omega^2/\pi^2c^3$.

essentially the same across each unit cell inside the two outer rings of air-voids, is suppressed by one order of magnitude at the center of the air-voids, and is slightly enhanced in the background. Outside the cluster in the jacket, the 3D LDOS rapidly falls to its free-space value.

The 3D LDOS is shown at the center of the cluster as a function of frequency in Fig. 8, both with and without an air-jacket for comparison. This again shows the effect of the jacket to be small. With the jacket, the 3D LDOS exhibits the same band gap signature with an increase in suppression with frequency inside the in-plane band gaps, strongest suppression at the top of the complete in-plane band gap, followed by a sharp jump above the gap. The jacket does, however, sharpen the features in the 3D LDOS. The maximum suppression is slightly stronger and is $\rho/\rho_0=1/12.5$ at $\omega d/2\pi c=0.449$ with the jacket, compared to $\rho/\rho_0=1/10.4$ at $\omega d/2\pi c=0.441$ without. The band-edge jump is sharper and

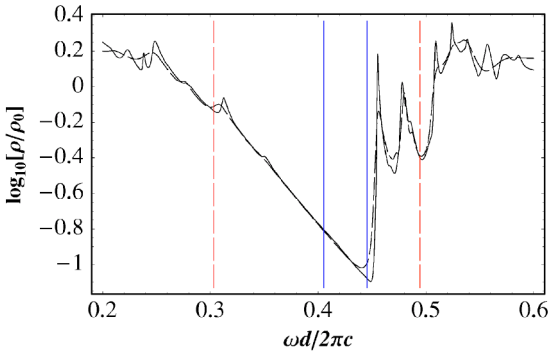

FIG. 8. 3D LDOS vs frequency in macroporous silicon (see Fig. 7) at $(x,y)/d=(0.0,0.0)$ with an air-jacket (solid line) and without (dashed line). The inner pair of vertical lines indicates the edges of the in-plane TM gap and the outer pair indicates the edges of the TE gap.

is $\delta\rho=1/19.2$ over $\delta\,\omega d/2\pi c=0.0065$ with the jacket, compared to $\delta\rho=1/7.6$ over $\delta\,\omega d/2\pi c=0.0155$ without. The jacket also generally sharpens the oscillations in the 3D LDOS.

The minor impact of the jacket on the 3D LDOS is largely attributable to the size of the cluster. The 3D LDOS was earlier shown to saturate rapidly with cluster size and is the same inside the two outermost rings of air-voids regardless of cluster size [35]. This is because the 2D periodicity of the 2D PC only partially affects the 3D emission from a point-source. As a consequence of the upward sloping out-of-plane band structure (Fig. 6), emission from the source at small propagation angles is affected by the in-plane band structure at frequencies at and immediately below the frequency of interest. Summing over these propagation angles (or in-plane frequencies) tends to dilute the impact of the 2D periodicity. The 2D periodicity has no impact at large propagation angles, and summation over the index-guided modes provides a foundation to the 3D LDOS that is more concentrated in the background than in the air-voids as the index-guided modes concentrate in the high dielectric region. The potential suppression of the 3D LDOS in 2D PCs is thus limited. The cluster examined is sufficiently large for the 3D LDOS to be robust and therefore for the presence of the jacket to have only a minor effect.

The jacket radius for a given cluster also needs to be considered. With the air-jacket, there is a discrete spectrum of bound modes whose number increases with the jacket radius. Clearly, the larger the jacket radius, the less significant is the change in the 3D LDOS. However, given that a closely fitting jacket on a moderately sized cluster has been shown to have a minor impact, it is reasonable to expect that the 3D LDOS rapidly converges to that in the infinite silicon background case with increasing jacket radius.

3. Bound and radiation components

The 3D LDOS is indicative of the angle-integrated spontaneous emission rate. Spontaneous emission rates in PCs also depend on emission angle because associated with the Bloch modes are directional Bloch vectors. Although the air-jacket does not significantly change the 3D LDOS, it allows 3D LDOS to be separated into its radiation and bound components. The radiation component is for emission into radiation modes that are oscillatory in air (see Fig. 6). Experimentally, this component gives the spontaneous emission rate integrated over all angles outside the cluster in the air-jacket. The bound component is for emission into bound modes that are evanescent in air and gives the spontaneous emission rate at the two opposing ends of the fiberlike structure. The radiation component at the center of the cluster is shown in Fig. 9, along with the total 3D LDOS for comparison. The difference between these two is indicative of the bound component. As all emission in free-space is into radiation modes, the free-space LDOS remains an appropriate reference for the radiation component. Inside the TE gap, the radiation component drops rapidly with frequency and is suppressed by $\rho/\rho_0=1/500$ at the bottom of the complete in-plane gap. Although almost all of the radiation modes are covered inside the complete gap, suppression ceases to grow further.

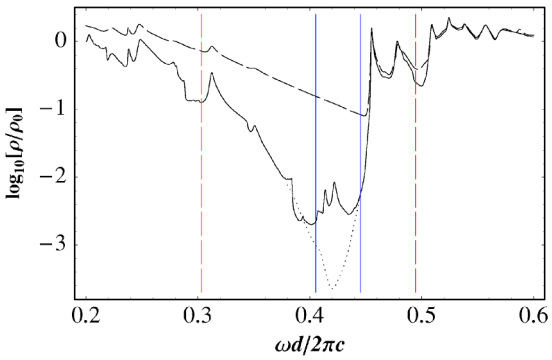

FIG. 9. Radiation component of the 3D LDOS at $(x,y)/d=(0.0,0.0)$ in macroporous silicon (Fig. 7). The radiation component for $N_c=37$ is plotted as a solid line, along with the total 3D LDOS, plotted as a dashed line. The radiation component near the complete gap for $N_c=61$ is also plotted as a dotted line.

This is attributable to the finite size of the structure, and obtaining further suppression requires a larger structure. The radiation component for $N_c=61$ cylinders (i.e., 4 rings) is also shown in the figure for frequencies near the complete gap. Suppression continues to grow inside the gap with a maximum suppression of $\rho/\rho_0=1/5000$ near the middle of the gap. Stronger suppression is likely in a larger structure. While the radiation component does not saturate rapidly with cluster size like the total 3D LDOS, these two results are not inconsistent because the radiation component is making a very small contribution to the total.

The suppression of the radiation component is strongest when the pseudogap covers all radiation modes. The 2D PC then behaves like an omnidirectional mirror [78] and only supports bound modes. Omnidirectional reflectance has been studied both theoretically and experimentally in multilayer film [78] and the Bragg fiber [79], which is composed of alternating dielectric rings to achieve periodicity in the radial direction. Omnidirectional mirror behavior in spontaneous emission where only emission into bound modes is supported has also been studied in multilayer film [38].

At the top of the complete in-plane gap, a high density of radiation modes with $\beta\approx 0$ (Fig. 6) is suddenly encountered and the radiation component rises rapidly. Dispersion is low in the β-direction at the top of the complete gap, resulting in the β content in the radiation component fanning out rapidly from $\beta\approx 0$ as frequency increases. Above the complete gap, the radiation comprises nearly the total 3D LDOS, while the bound component becomes suppressed as the pseudogap moves from the oscillatory region into the evanescent region. However, the pseudogap only ever covers a narrow range of evanescent modes and the impact on the bound component is not as significant as it is on the radiation component. The very heavy suppression of the radiation component of the 3D LDOS at the top of the complete gap, followed by the sudden burst of emission into radiation modes propagating near in-plane is perhaps the most striking band gap effect in spontaneous emission in 2D PCs.

4. Projected local density of states

The 3D PLDOS for dipoles oriented in the z, x, and y directions [i.e., $\rho(\mathbf{r},\omega,\hat{\mathbf{z}})$, $\rho(\mathbf{r},\omega,\hat{\mathbf{x}})$, and $\rho(\mathbf{r},\omega,\hat{\mathbf{y}})$] are

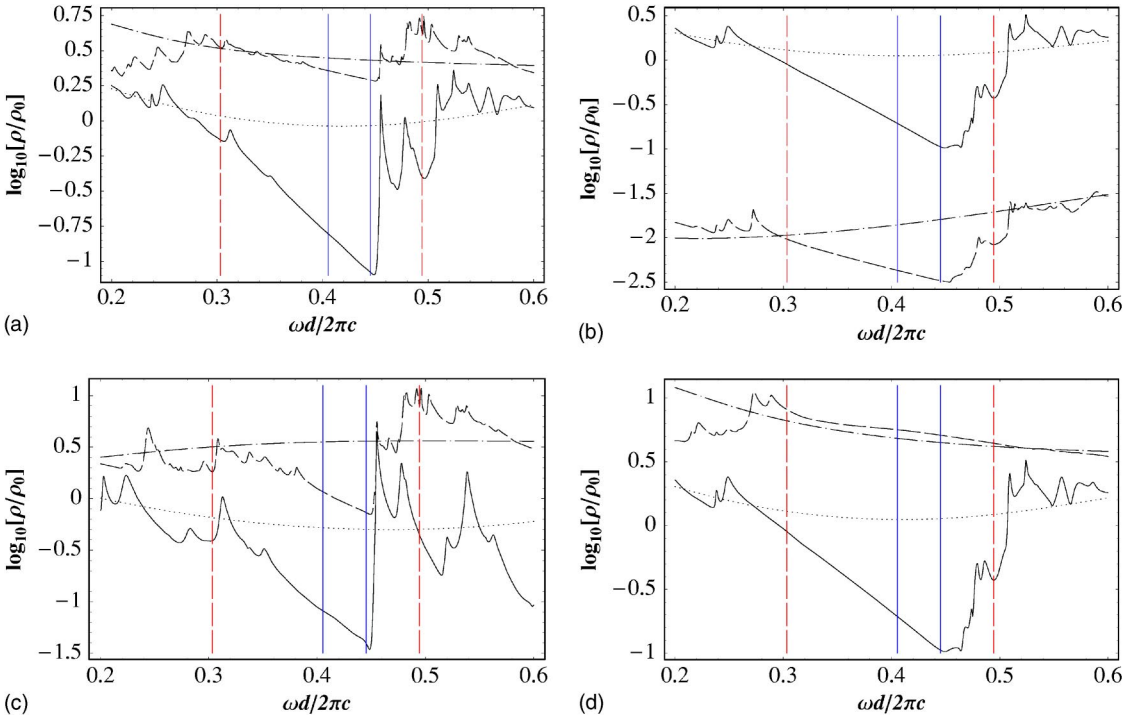

FIG. 10. The 3D LDOS (a) and 3D PLDOS for an *x*-oriented dipole (b), a *z*-oriented dipole (c), and at a *y*-oriented dipole (d) in an hexagonal cluster of air-voids (Fig. 7) at $(x,y)/d=(0.0,0.0)$ (solid line) and (0.5,0.0) (dashed line). Also shown are the 3D LDOS and 3D PLDOS at the center of a single isolated air-void in a silicon background (dotted line) and at $(x,y)/d=(0.5,0.0)$, directly between two adjacent air-voids positioned at $(x,y)/d=(0.0,0.0)$ and $(x,y)/d=(1.0,0.0)$ in a silicon background (dash-dot line).

shown in Fig. 10. The 3D PLDOS at the center of the cluster is plotted along with the 3D PLDOS at the center of a single air-void in an infinite silicon background, but otherwise with the same parameters, to isolate band gap effects from single scatterer effects. The 3D LDOS is included and is simply the sum of these three 3D PLDOS values at the coordinates shown. At the center of the cluster, the 3D PLDOS for all three dipoles exhibits the same band gap signature as the 3D LDOS, falling smoothly and continuously inside the TE gap with maximum suppression at the top of the complete gap. The maximum suppression of $\rho/\rho_0=1/29.1$ for $\rho(\mathbf{r},\omega,\hat{\mathbf{z}})$ is, however, significantly higher than the $\rho/\rho_0=1/9.7$ for $\rho(\mathbf{r},\omega,\hat{\mathbf{x}})$. Due to the symmetry of the structure, $\rho(\mathbf{r},\omega,\hat{\mathbf{x}})$ and $\rho(\mathbf{r},\omega,\hat{\mathbf{y}})$ are virtually identical. Above the complete gap, $\rho(\mathbf{r},\omega,\hat{\mathbf{z}})$ jumps sharply higher by $\delta\rho=129$ over $\delta\omega d/2\pi c=0.0066$, while $\rho(\mathbf{r},\omega,\hat{\mathbf{x}})$ climbs gradually. Above the TE gap, $\rho(\mathbf{r},\omega,\hat{\mathbf{x}})$ jumps higher, but $\rho(\mathbf{r},\omega,\hat{\mathbf{z}})$ is unaffected. Thus, the 3D PLDOS at the center of the cluster undergoes both relatively strong suppression and modulation with frequency because its three 3D PLDOS components each undergo similar changes and reinforce each other. For a single isolated air-void in a dielectric background, single scatterer effects are minor and comparing the 3D PLDOS and 3D LDOS in the cluster with those in the isolated air-void shows the suppression inside the in-plane gaps to be a genuine band gap effect. Outside the gaps, the 3D PLDOS and 3D LDOS in the cluster return to varying moderately around those of the single air-void.

The connection between $\rho(\mathbf{r},\omega,\hat{\mathbf{z}})$ and TM modes, and $\rho(\mathbf{r},\omega,\hat{\mathbf{x}})$ and $\rho(\mathbf{r},\omega,\hat{\mathbf{y}})$, and TE modes, can be explained as follows. By Eq. (3), $\rho(\mathbf{r},\omega,\hat{\mathbf{z}})$ is determined by the *z*-component of the modal fields, while $\rho(\mathbf{r},\omega,\hat{\mathbf{x}})$ and $\rho(\mathbf{r},\omega,\hat{\mathbf{y}})$ are determined by the *x* and *y*-components, respectively. For in-plane propagation ($\beta=0$), the former corresponds to TM modes, while the latter corresponds to TE modes. For $\beta>0$, the modes are no longer decoupled, and the modes emanating from the in-plane TM modes acquire *x* and *y*-components, while the modes emanating from the in-plane TE modes acquire a *z*-component. As shown in Fig. 6, the integration over β effectively draws in the in-plane band structure at and below the frequency of interest. However, for β small near the in-plane band gaps, dispersion in the β direction is low, and it is reasonable to expect that the in-plane band structure immediately below will have the most significant impact on the 3D PLDOS. Consequently, $\rho(\mathbf{r},\omega,\hat{\mathbf{z}})$ remains closely tied to the in-plane TM band structure, while $\rho(\mathbf{r},\omega,\hat{\mathbf{x}})$ and $\rho(\mathbf{r},\omega,\hat{\mathbf{y}})$ remain closely tied to the in-plane TE band structure.

The 3D PLDOS in the background at $(x,y)/d=(0.5,0.0)$, between two adjacent air-voids at the center of the cluster, is also shown in Fig. 10. Along with this, the 3D PLDOS is plotted between the two adjacent air-voids without the surrounding cluster and jacket, again to isolate band gap effects from local field effects. In the cluster, $\rho(\mathbf{r},\omega,\hat{\mathbf{z}})$ is enhanced in the background with a band gap effect comparable to that in the center, but far less dramatic. There is little difference between $\rho(\mathbf{r},\omega,\hat{\mathbf{y}})$ in the cluster and between two isolated air-voids, and it is enhanced with no discernable band gap effect. In contrast, $\rho(\mathbf{r},\omega,\hat{\mathbf{x}})$ is heavily suppressed, again like it is between two isolated air-voids, with a small superim-

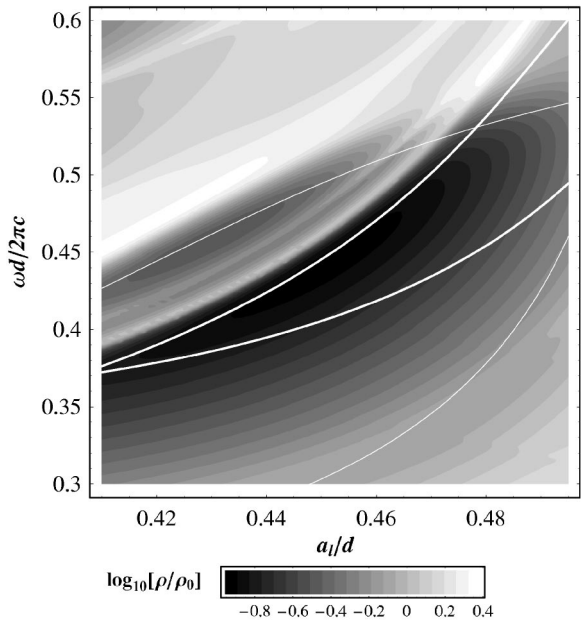

FIG. 11. 3D LDOS vs frequency and a_l in macroporous silicon at $(x,y)/d=(0.0,0.0)$. The cluster is composed of $N_c=19$ air-voids in an infinite silicon background. The plot is overlaid with the corresponding gap map (white lines), with thick lines indicating the edges of the TM gap and thin lines indicating the edges of the TE gap.

posed band gap effect so that at the top of the complete in-plane gap, $\rho/\rho_0=1/280$. As a consequence of these three results, the 3D LDOS is moderately enhanced in the background similarly to $\rho(\mathbf{r},\omega,\hat{\mathbf{z}})$, but with smaller variations.

While band gap effects are most significant in the air-voids, local field effects are most significant in the background. The highly polarized results in the background are due to the very narrow dielectric vein between two close adjoining air-voids. This leads to a strong anisotropy in the depolarization factors for the field parallel to the x-oriented dipole and the fields parallel to the z- and y-oriented dipoles. It is beyond the scope of this paper to evaluate these depolarization factors. However, spontaneous emission in elliptical particles was examined recently [80], and the results bear some consideration. The limiting depolarization factor for eccentricity $e\rightarrow 1$ (i.e., infinite semimajor axis) for the field parallel to the semiminor axis is $f\rightarrow 1/n^4$, while for the semimajor axis $f\rightarrow 1$. This suggests that the spontaneous emission rate for a dipole oriented parallel to the narrow side of a highly elongated dielectric region will be heavily suppressed, while for a dipole parallel to the long side, the spontaneous emission rate will be relatively unchanged. It is also consistent with heavy suppression in the x-oriented dipole while the z-oriented dipole is relatively unaffected.

5. Exploration of parameter space

Macroporous silicon has so far been considered with a fixed air-void radius of $a_l/d=0.45$. Figure 11 shows how the 3D LDOS changes when a_l/d is varied. The plot depicts the 3D LDOS at the center of the cluster as a function of frequency, as in Fig. 8. As the 3D LDOS is essentially the same

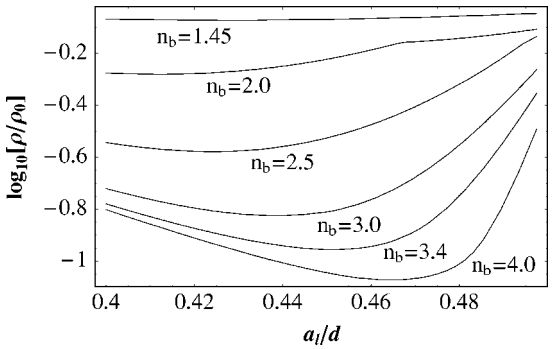

FIG. 12. Maximum suppression in the 3D LDOS vs a_l (re. Fig. 11) for given n_b.

inside the two outermost rings of air-voids, regardless of cluster size, and the jacket has a minor effect, a cluster of $N_c=19$ air-voids in an infinite silicon background is used for efficient modeling. The gap map, which shows the TM and TE band gaps as a function of a_l/d, is also plotted. The band gap signature observed in Fig. 8 is essentially reproduced for varying a_l/d. When the top of the TE gap is above the top of the TM gap, the 3D LDOS also exhibits a second minor trough. Although the TM gap continues to expand with a_l/d and the complete gap is widest at $a_l/d=0.473$, the greatest suppression occurs at $a_l/d=0.45$ where the TE gap is widest.

The most distinct feature of the 3D LDOS in macroporous silicon is the strong suppression of approximately one order of magnitude at the top of the complete in-plane gap. Figure 12 shows how this feature depends on the background refractive index. The maximum suppression for a given a_l/d is plotted for refractive indices of several important PC materials. Plots are shown for the refractive indices of glasses that have been used to fabricate fibers: $n_b=1.45$ (silica glasses), 2.0 (high lead concentration glasses), and 2.5 (chalcogenide glasses) [81]; and for materials that have been used or may be used to fabricate PCs: 3.0 (Al_2O_3 [49]), 3.4 (silicon [50] and GaAs), and 4.0 (germanium). The maximum suppression and the a_l/d at which this occurs are also shown in Table II. As n_b increases, the maximum suppression increases, and the a_l/d at which this occurs are also increases. This result is again closely tied to the band structure. As n_b increases in this type of structure, both the width of the in-plane gaps and the a_l/d at which these are widest on the gap map also in-

TABLE II. Minima in the 3D LDOS shown in Fig. 12. The air-void radius (a_l/d) and the maximum suppression ($\log[\rho/\rho_0]$) for each n_b is tabulated, along with the frequency ($\omega_d/2\pi c$) at which it occurs.

n_b	a_l/d	$\log[\rho/\rho_0]$	$\omega d/2\pi c$
1.45	0.4300	−0.0724	0.506
2.00	0.4125	−0.2800	0.496
2.50	0.4250	−0.5777	0.472
3.00	0.4375	−0.8246	0.454
3.40	0.4500	−0.9551	0.440
4.00	0.4650	−1.0718	0.424

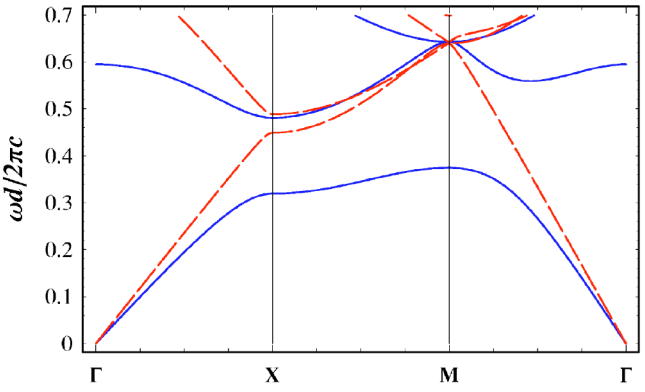

FIG. 13. 2D band structure for a square array of dielectric cylinders in air (PC2). The array parameters are $a_l/d=0.15$, $n_l=3.0$, and $n_b=1.0$. The TM modes are shown as a solid line and the TE modes are shown as a dashed line.

crease. However, with only 2D confinement, maximum suppression is not significantly stronger when the refractive index contrast is high, and is effectively limited to $\rho/\rho_0 \approx 1/15$ in a 2D PC.

B. Square cluster of dielectric cylinders in air (PC2)

1. Band structure

The second structure examined is a square cluster of dielectric cylinders in an air background (PC2). The main emphasis is on a cluster of cylinders of radius $a_l/d=0.15$ and refractive index $n_l=3.0$ in an air background ($n_b=1.0$). The in-plane band structure for the underlying lattice is shown in Fig. 13. In contrast to the previous 2D PC, TM gaps are favored in this type of 2D PC [8] and it has a wide TM gap in the frequency range $\omega d/2\pi c=0.375-0.481$ ($\Delta\omega/\omega_0=24.9\%$), but no TE gaps.

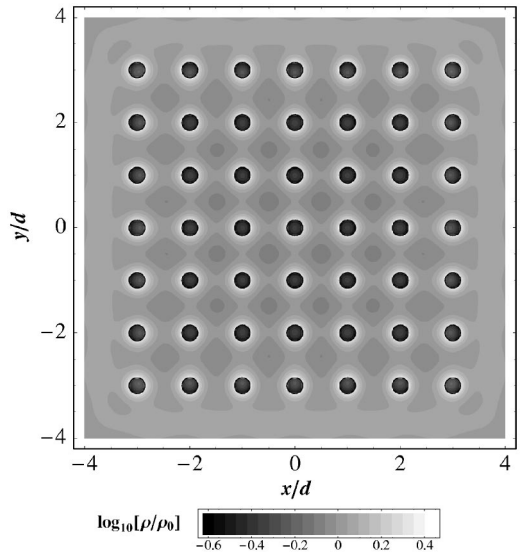

FIG. 14. 3D LDOS across the plane of a square cluster of dielectric cylinders in air. The frequency is $\omega d/2\pi c=0.48$ and the cluster parameters are $N_c=49$, $a_l/d=0.15$, $n_l=3.0$, and $n_b=1.0$.

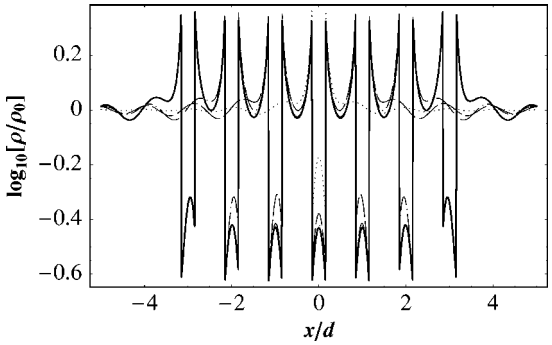

FIG. 15. 3D LDOS along the x-axis for varying cluster sizes. The section of Fig. 14 at $\omega d/2\pi c=0.48$ with $N_c=49$ is shown (solid-bold line) along with $N_c=1$ (dotted line), 9 (dashed line), and 25 (dash-dot line), but otherwise using the same parameters.

2. Local density of states

The 3D LDOS across the plane of a cluster of $N_c=49$ dielectric cylinders is shown in Fig. 14. The frequency is $\omega d/2\pi c=0.48$, and lies just below the top of the TM gap. Like PC1 (see Fig. 7), the 3D LDOS is essentially the same across each unit cell in the cluster, particularly inside the outermost square-ring of cylinders. It is also suppressed inside the cylinders, but the most significant effects occur at the cylinder surface. The 3D LDOS is suppressed by a factor of $\rho/\rho_0=1/2.7$ at the center, strengthening a little to $\rho/\rho_0=1/4.2$ just inside the cylinder surface. At the surface, the 3D LDOS then jumps sharply by almost one order of magnitude and is enhanced by $\rho/\rho_0=2.1$ just outside, before falling to near-zero between the cylinders.

The dependence of the 3D LDOS on cluster size is demonstrated in Fig. 15 where it is shown in one cylinder ($N_c=1$) and clusters of one ($N_c=9$), two ($N_c=25$), and three ($N_c=49$) square rings of cylinders. The variation of the 3D LDOS with position inside the cluster shown in Fig. 14 is also made clearer. The figure shows that the 3D LDOS in a single cylinder is significant, and it is suppressed by a factor of $\rho/\rho_0=1/1.5$ at the center, growing to $\rho/\rho_0=1/2.4$ inside the cylinder surface and then jumping just outside to be enhanced by $\rho/\rho_0=2.3$. Adding square rings of cylinders results in stronger suppression inside the cylinders, but again the suppression saturates rapidly with cluster size, and the maximum suppression is achieved once there are two or more rings. The 3D LDOS is also essentially the same with distance from the outer boundary, regardless of cluster size.

The significance of cluster size is also demonstrated in Fig. 16 where the 3D LDOS is shown at the surface of the central cylinder of the cluster as a function of frequency. This is done for the same clusters as in Fig. 15. The result for a single cylinder is again shown to be significant, and the 3D LDOS is suppressed at low frequencies, rises approaching the bottom of the TM gap, falls inside the gap with a minimum near the top of the gap, then rises again above the gap. In a cluster of cylinders, the band structure manifests itself as suppression in the 3D LDOS relative to that in the single cylinder inside the TM gap, and enhancement surrounding the gap. The band gap signature is similar to that for PC1, with growing suppression inside the in-plane gap and maxi-

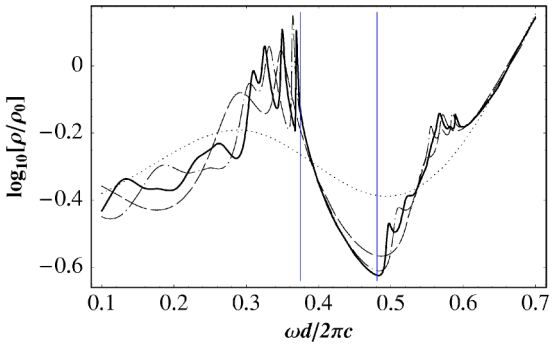

FIG. 16. 3D LDOS vs frequency for varying cluster sizes. The 3D LDOS is taken at $(x,y)/d=(0.15,0.0)$ (re. Fig. 14) for $N_c=49$ (solid-bold line), $N_c=1$ (dotted line), $N_c=9$ (dashed line), and $N_c=25$ (dash-dot line). The pair of vertical lines indicates the edges of the in-plane TM gap.

mum suppression at the top. However, with a gap in only one polarization, the maximum suppression is well below the one order of magnitude obtained in macroporous silicon. The rapid saturation in the suppression of the 3D LDOS at the top of the TM gap with cluster size is also again clear.

At low frequencies below the TM gap, the 3D LDOS exhibits significant and rapid oscillations whose number and density depend on the cluster size. These are attributed to a long-wavelength regime where the whole cluster behaves like a single homogenized scatterer, possessing a frequency-dependent effective refractive index. The local peaks in the 3D LDOS represent resonances, whose number and location depend upon the size and effective index of the structure. Above the TM gap, this size effect is far less significant, and at high frequencies the 3D LDOS in a cluster is close to that in a single cylinder.

3. Projected local density of states

In Fig. 17, the 3D LDOS is shown along with the 3D PLDOS for dipoles oriented in the z, x, and y directions. The 3D LDOS and 3D PLDOS on the surface of a single isolated dielectric cylinder are also shown to isolate band gap effects from single cylinder effects. The close connection between $\rho(\mathbf{r},\omega,\hat{\mathbf{z}})$ and TM modes described earlier for PC1 is again evident. The band gap effect in $\rho(\mathbf{r},\omega,\hat{\mathbf{z}})$ is strongest in the background at $(x,y)/d=(0.5,0.0)$ where $\rho(\mathbf{r},\omega,\hat{\mathbf{z}})$ drops significantly inside the TM gap and is suppressed by $\rho/\rho_0=1/6.1$ at the top of the gap. With no TE gap, there are no significant band structure effects in $\rho(\mathbf{r},\omega,\hat{\mathbf{x}})$ and $\rho(\mathbf{r},\omega,\hat{\mathbf{y}})$. Both are heavily suppressed by $\rho/\rho_0=1/18.6$ inside the cylinders at $\omega d/2\pi c=0.1$, but this is a single cylinder effect.

In the long wavelength regime in a single cylinder, there is strong polarization anisotropy between dipoles oriented parallel and perpendicular to the cylinder axis. This is again due to the strong anisotropy in the corresponding depolarization factors, discussed earlier for PC1. In fact, this result concurs with recent experiment [82]. The polarized photoluminescence (PL) in indium phosphide nanowires ($n_l=3.5$) was measured using a polarized pump beam. This was done for polarization parallel to the cylinder axis, probing $\rho(\mathbf{r},\omega,\hat{\mathbf{z}})$, and perpendicular, probing $\rho(\mathbf{r},\omega,\hat{\mathbf{x}})$, in the long wavelength regime. Order-of-magnitude polarization anisotropy was observed, consistent with the results in Fig. 17.

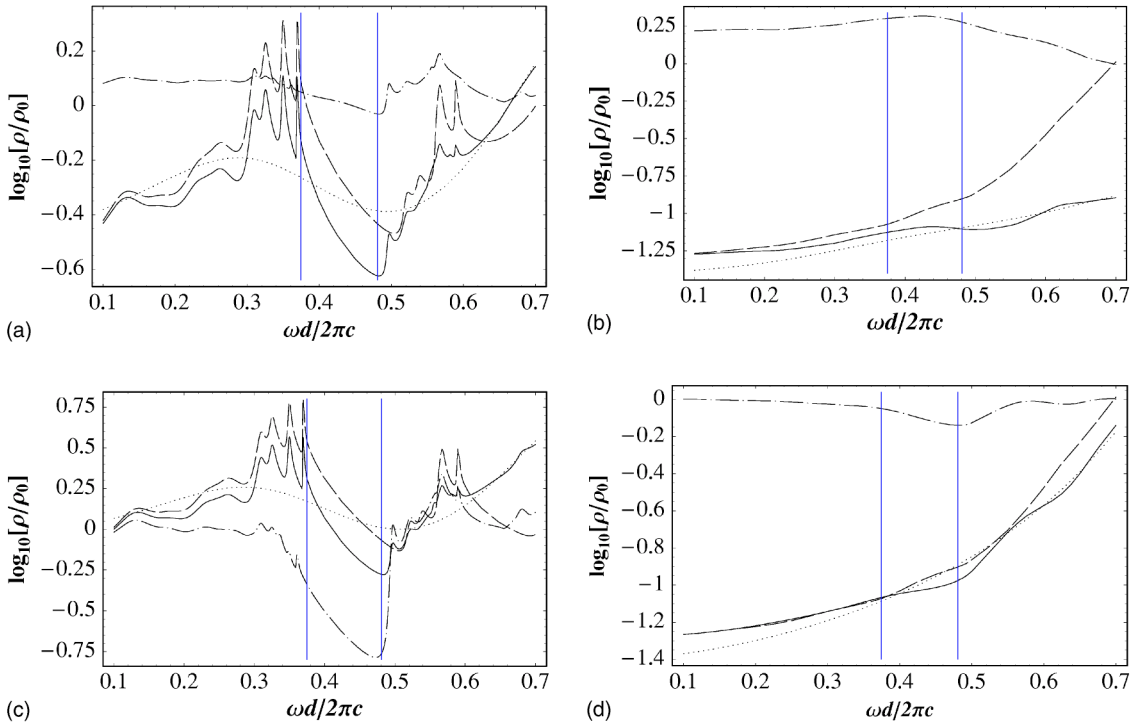

FIG. 17. 3D LDOS (a) and 3D PLDOS for an x-oriented dipole (b), a z-oriented dipole (c), and a y-oriented dipole (d) at $(x,y)/d=(0.15,0.0)$ (solid line), (0.0, 0.0) (dashed line), and (0.5, 0.0) (dash-dot line). Also shown are the 3D LDOS and 3D PLDOS for one dielectric cylinder at (0.15,0.0) (dotted line).

Similar to PC1, band gap effects in PC2 are most significant in the low dielectric region, while the most significant local field effects occur in the high dielectric region. The interesting features in the 3D LDOS in PC2 are largely attributable to the TM band structure through $\rho(\mathbf{r},\omega,\hat{\mathbf{z}})$. While the suppression in $\rho(\mathbf{r},\omega,\hat{\mathbf{z}})$ is strongest at $(x,y)/d=(0.5,0.0)$, this does not occur in the 3D LDOS because there is no support from $\rho(\mathbf{r},\omega,\hat{\mathbf{x}})$ and $\rho(\mathbf{r},\omega,\hat{\mathbf{y}})$. The suppression in the 3D LDOS is strongest at the cylinder surface where $\rho(\mathbf{r},\omega,\hat{\mathbf{z}})$ is still significantly suppressed, and $\rho(\mathbf{r},\omega,\hat{\mathbf{x}})$ and $\rho(\mathbf{r},\omega,\hat{\mathbf{y}})$ are also suppressed.

VI. DISCUSSION AND CONCLUSIONS

The 3D Green's tensor is a versatile tool that can be used to obtain the 3D LDOS, but a method is required that gives the real and imaginary components separately and to high accuracy, and keeps them apart from the divergent real component at the source position. By employing a combination of a Fourier contour integral and a Rayleigh-multipole method, a highly efficient and accurate approach has been demonstrated for calculating the 3D Green's tensor in 2D PCs composed of cylinders. The multipole method uses a field expansion that is consistent with the geometry of the problem, giving it several major advantages over the alternatives. First, the boundary conditions are enforced analytically rather than through a Fourier series, avoiding the convergence challenge posed by high dielectric contrast for plane-wave methods. Second, a simple semianalytic expression for the fields is obtained with the source field separate from the scattered field. Third, an elegant identity is obtained from which the eigenvalue problem can be solved and the field coefficients determined with a single matrix inversion. Fourth, convergence in the field expansions is superior, allowing EM problems in complex structures to be investigated on a desktop computer. This also allows the large parameter space of PCs including lattice geometry, cylinder size, and refractive index contrast, to be explored. Finally, with well-developed theory for Bessel functions in complex space, the Fourier transform required for the 3D Green's tensor can be evaluated efficiently on an appropriately chosen complex contour, giving the real and imaginary components separately. This also allows the approach to deal with the complex parameters of materials with gain or loss.

The 3D Green's tensor was used to perform a large-scale investigation into spontaneous emission in 2D PCs. A comprehensive collection of LDOS results has been produced and reconciled with the band structure. The results have also been compared to those for a single scatterer to isolate genuine band gap effects from local field effects. The 3D LDOS has been examined as a function of frequency and position, along with the dependence on PC parameters like lattice configuration, cylinder radius, and refractive index contrast. The 3D LDOS has also been decomposed into its radiation and bound components, and also the 3D PLDOS, which are both more sensitive probes of band gap effects.

The first structure examined was a 2D PC composed of a hexagonal cluster of air-voids in a dielectric background (PC1). This 2D PC has a complete in-plane band gap that manifests itself as a distinct signature in the 3D LDOS at the center of the air-voids. The suppression in the 3D LDOS, and spontaneous emission, get progressively stronger with frequency inside the TE gap and reach a maximum of one order of magnitude at the top of the complete gap. The 3D LDOS then jumps sharply higher above the gap. Enclosing the cluster with an air-jacket to form a fiberlike 2D PC does not significantly change this signature. However, the jacket is an important extension because it is a more realistic geometry than an infinite silicon background, and it means that PC fibers, which are an important class of 2D PC, can be modeled. Furthermore, the jacket allows the 3D LDOS to be separated into its radiation and bound components. Experimentally, the radiation component is detected outside the cluster in the transverse direction, while the bound component is detected at the ends of the 2D PC. In 2D PCs like macroporous silicon, which have a wide complete in-plane gap, the radiation component can be almost completely suppressed just below the top of the complete gap. At the top, a high density of radiation modes propagating close to in-plane is suddenly encountered, and the radiation component jumps sharply. This result would be observed as the radiation component rapidly switching on about the edge of the gap and provides perhaps the strongest experimental measure of band gap effects in spontaneous emission in 2D PCs.

The band gap signature in the 3D LDOS also occurs in the 3D PLDOS. At the center of the air-voids, $\rho(\mathbf{r},\omega,\hat{\mathbf{z}})$ exhibits the strongest features and is suppressed by a factor of 30 at the top of the complete gap before rapidly jumping over two orders of magnitude higher above the gap. The strongest suppression in the 3D PLDOS occurs in the background between two adjacent air-voids where $\rho(\mathbf{r},\omega,\hat{\mathbf{x}})$ is suppressed by more than two orders of magnitude over a large frequency range. However, this is a local field effect attributable to the narrow width of the dielectric vein rather than a band gap effect. The dependence of the band gap signature on air-void radius and background refractive index was also examined. As might be expected, the strength of the suppression depends on the width of the gaps. As the air-void radius increases, the TM gap widens while the TE gap widens then narrows, and the suppression is strongest when both gaps are wide. As the refractive index increases, the complete gap widens, however suppression is essentially limited to one order of magnitude for realistic values, again because the periodicity of the 2D PC only affects two of the three dimensions of wave propagation.

The second structure examined was a 2D PC composed of a square cluster of dielectric cylinders (PC2). In contrast to PC1, PC2 has a large TM gap, but does not have a complete in-plane gap. The band gap produces a signature in the 3D LDOS similar to that in PC1, but with no complete in-plane gap, suppression is limited to about a factor of 5. Also, the 3D LDOS increases gradually above the gap rather than jumping sharply. This signature again occurs inside the cylinders, but is strongest at the cylinder surface rather than the center. The signature is strongest in $\rho(\mathbf{r},\omega,\hat{\mathbf{z}})$ because of its close connection with the TM band structure, but the suppression at the top of the TM gap remains below one order of magnitude. In contrast to PC1, single cylinder effects are significant in PC2 and are attributable to confinement in a

dielectric cylinder in air. The 3D LDOS in one cylinder shows relatively strong variations with position and frequency that are similar to those in a cluster, but smaller. While there are no significant band gap effects in $\rho(\mathbf{r},\omega,\hat{\mathbf{x}})$ and $\rho(\mathbf{r},\omega,\hat{\mathbf{y}})$, both are suppressed by well over one order of magnitude at long wavelengths.

ACKNOWLEDGMENT

Support from the Center for Ultra-high Bandwidth Devices for Optical Systems (CUDOS) funded by the Australian Research Council (ARC) is acknowledged.

APPENDIX A: HOMOGENEOUS GREEN'S TENSOR

The homogeneous 3D Green's tensor, $\mathbf{G}_n$, presented in the following is obtained using Eq. (13) in Eq. (11). Noting that $\mathbf{G}_n^E$ is a symmetric tensor while $\mathbf{G}_n^H$ is an antisymmetric tensor, only the upper-triangular components are shown. Also, only the Fourier transform is shown, and $\mathbf{G}_n$ can be obtained as in Sec. III. The components of $\tilde{\mathbf{G}}_n^E$ in Cartesian coordinates are

$$\tilde{G}^E_{nzz} = -\frac{i}{4}\left(1-\frac{\beta^2}{(kn)^2}\right)H_0^{(1)}(k_\rho|\boldsymbol{\rho}-\boldsymbol{\rho}'|),$$

$$\tilde{G}^E_{nxz} = -\frac{\beta k_\rho}{4(kn)^2}H_1^{(1)}(k_\rho|\boldsymbol{\rho}-\boldsymbol{\rho}'|)\cos\,\phi_{\rho\rho'},$$

$$\tilde{G}^E_{nyz} = -\frac{\beta k_\rho}{4(kn)^2}H_1^{(1)}(k_\rho|\boldsymbol{\rho}-\boldsymbol{\rho}'|)\sin\,\phi_{\rho\rho'},$$

$$\tilde{G}^E_{nxx} = -\frac{i}{8}\left[\left(1+\frac{\beta^2}{(kn)^2}\right)H_0^{(1)}(k_\rho|\boldsymbol{\rho}-\boldsymbol{\rho}'|) + \frac{k_\rho^2}{(kn)^2}H_2^{(1)}(k_\rho|\boldsymbol{\rho}-\boldsymbol{\rho}'|)\cos\,2\phi_{\rho\rho'}\right],$$

$$\tilde{G}^E_{nyy} = -\frac{i}{8}\left[\left(1+\frac{\beta^2}{(kn)^2}\right)H_0^{(1)}(k_\rho|\boldsymbol{\rho}-\boldsymbol{\rho}'|) - \frac{k_\rho^2}{(kn)^2}H_2^{(1)}(k_\rho|\boldsymbol{\rho}-\boldsymbol{\rho}'|)\cos\,2\phi_{\rho\rho'}\right],$$

$$\tilde{G}^E_{nxy} = -\frac{ik_\rho^2}{4(kn)^2}H_2^{(1)}(k_\rho|\boldsymbol{\rho}-\boldsymbol{\rho}'|)\cos\,\phi_{\rho\rho'}\sin\,\phi_{\rho\rho'}, \quad \text{(A1)}$$

where $\phi_{\rho\rho'}=\arg(\boldsymbol{\rho}-\boldsymbol{\rho}')$. The nonzero components of $\tilde{\mathbf{G}}_n^H$ are

$$\tilde{G}^H_{nxz} = \frac{ik_\rho}{4}H_1^{(1)}(k_\rho|\boldsymbol{\rho}-\boldsymbol{\rho}'|)\sin\,\phi_{\rho\rho'},$$

$$\tilde{G}^H_{nyz} = -\frac{ik_\rho}{4}H_1^{(1)}(k_\rho|\boldsymbol{\rho}-\boldsymbol{\rho}'|)\cos\,\phi_{\rho\rho'},$$

$$\tilde{G}^H_{nxy} = \frac{\beta}{4}H_0^{(1)}(k_\rho|\boldsymbol{\rho}-\boldsymbol{\rho}'|). \quad \text{(A2)}$$

APPENDIX B: SOURCE COEFFICIENTS

The expressions for the source coefficients, K_m^l and Q_m^l, follow from using Graf's addition theorem to write

$$H_0^{(1)}(k_\rho|\boldsymbol{\rho}-\boldsymbol{\rho}'|)=\sum_{p=-\infty}^{\infty}H_p^{(1)}(k_\rho\rho_>)J_p(k_\rho\rho_<)e^{ip\,\arg(\boldsymbol{\rho}-\boldsymbol{\rho}')}, \quad \text{(B1)}$$

where $\rho_>=\max(|\boldsymbol{\rho}-\boldsymbol{\rho}_l|,|\boldsymbol{\rho}'-\boldsymbol{\rho}_l|)$ and $\rho_<=\min(|\boldsymbol{\rho}-\boldsymbol{\rho}_l|,|\boldsymbol{\rho}'-\boldsymbol{\rho}_l|)$. Also, the differentials in Eq. (15) are rewritten in terms of source coordinates using the reciprocity properties of $\mathbf{G}_n$, which gives $\mathcal{D}'^E_u=\mathcal{D}^E_u$ and $\mathcal{D}'^H_u=\mathcal{D}^H_u$. Applying these differentials to Eq. (B1) in the matrix then gives K_m^l, with nonzero components

$$K^{El}_{zm} = \left(1-\frac{\beta^2}{(kn)^2}\right)H_m^{(1)}(k_\rho\rho_{ls})e^{-im\phi_{ls}},$$

$$K^{El}_{xm} = -\frac{i\beta k_\rho}{2(kn)^2}[H^{(1)}_{m-1}(k_\rho\rho_{ls})e^{-i(m-1)\phi_{ls}} - H^{(1)}_{m+1} \times(k_\rho\rho_{ls})e^{-i(m+1)\phi_{ls}}],$$

$$K^{El}_{ym} = -\frac{\beta k_\rho}{2(kn)^2}[H^{(1)}_{m+1}(k_\rho\rho_{ls})e^{-i(m+1)\phi_{ls}} + H^{(1)}_{m-1} \times(k_\rho\rho_{ls})e^{-i(m-1)\phi_{ls}}],$$

$$K^{Hl}_{xm} = \frac{k_\rho}{2i}[H^{(1)}_{m+1}(k_\rho\rho_{ls})e^{-i(m+1)\phi_{ls}} + H^{(1)}_{m-1}(k_\rho\rho_{ls})e^{-i(m-1)\phi_{ls}}],$$

$$K^{Hl}_{ym} = -\frac{k_\rho}{2}[H^{(1)}_{m-1}(k_\rho\rho_{ls})e^{-i(m-1)\phi_{ls}} - H^{(1)}_{m+1}(k_\rho\rho_{ls})e^{-i(m+1)\phi_{ls}}], \quad \text{(B2)}$$

where $(\rho_{ls},\phi_{ls})=(\boldsymbol{\rho}_s-\boldsymbol{\rho}_l)$. The Q_m^l coefficients are similar with $H_m^{(1)}$ replaced by J_m. The expressions for K_m^0 and Q_m^0 are obtained upon setting $\boldsymbol{\rho}_l=\mathbf{0}$.

APPENDIX C: BOUNDARY CONDITIONS

The boundary conditions are determined here for a cylinder of radius a centered at the origin of a cylindrical coordinate system (z,ρ,ϕ). Quantities inside the cylinder are denoted "−," and those outside are denoted "+." The z-components of the fields in the vicinity of the cylinder surface are expressed as

$$V^{\pm}=\sum_{m=-\infty}^{\infty}[A_m^{V\pm}J_m(k_\rho^{\pm}\rho)+B_m^{V\pm}H_m^{(1)}(k_\rho^{\pm}\rho)]e^{im\phi}, \quad \text{(C1)}$$

where $V\in\{E,H\}$ and $k_\rho^{\pm}=\sqrt{k^2n_\pm^2-\beta^2}$. The boundary conditions are that the tangential field components, that is the z and ϕ components, be continuous at a cylinder surface. For example, for the z-components of the E field,

$$A_m^{E-} J_m^- + B_m^{E-} H_m^- = A_m^{E+} J_m^+ + B_m^{E+} H_m^+, \tag{C2}$$

where $J_m^- = J_m(k_\rho^- a)$, etc. The linear relations for the coefficients that result from the boundary conditions can be written

$$\mathbf{A}^- = \mathbf{T}^- \mathbf{A}^+ + \mathbf{R}^- \mathbf{B}^-,$$

$$\mathbf{B}^+ = \mathbf{R}^+ \mathbf{A}^+ + \mathbf{T}^+ \mathbf{B}^-, \tag{C3}$$

where **R** and **T** are the reflection and transmission matrices, respectively. The exterior reflection matrix is

$$\mathbf{R}^+ = \begin{bmatrix} R_m^{EE+} & R_m^{EH+} \\ R_m^{HE+} & R_m^{HH+} \end{bmatrix}, \tag{C4}$$

with

$$R_m^{EE+} = \frac{1}{\delta_m}[(\alpha_{J^-H^+} - \alpha_{H^+J^-})(n_-^2 \alpha_{J^-J^+} - n_+^2 \alpha_{J^+J^-}) - m^2 J^+ H^+ J^{-2} \tau^2],$$

$$R_m^{EH+} = \frac{1}{\delta_m} m J^{-2} \frac{k_\rho^-}{k k_\rho^+} \frac{2i}{\pi a} \tau,$$

$$R_m^{HE+} = k^2 n_+^2 R_m^{EH+},$$

$$R_m^{HH+} = \frac{1}{\delta_m}[(\alpha_{J^-J^+} - \alpha_{J^+J^-})(n_-^2 \alpha_{J^-H^+} - n_+^2 \alpha_{H^+J^-}) - m^2 J^+ H^+ J^{-2} \tau^2], \tag{C5}$$

and

$$\delta_m = (\alpha_{H^+J^-} - \alpha_{J^-H^+})(n_-^2 \alpha_{J^-H^+} - n_+^2 \alpha_{H^+J^-}) + m^2 J^{-2} H^{+2} \tau^2,$$

$$\tau = \frac{k_\rho^+}{k k_\rho^-} \left(\frac{k_\rho^{-2}}{k_\rho^{+2}} - 1 \right) \frac{\beta}{a},$$

and where $\alpha_{J^-H^+} = J'^-_m H_m^+ k_\rho^+$, etc. Similarly, the components of the exterior transmission matrix are

$$T_m^{EE+} = \frac{1}{\delta_m} \frac{k_\rho^+}{k_\rho^-} n_-^2 (\alpha_{J^-H^+} - \alpha_{H^+J^-}) \frac{2i}{\pi a},$$

$$T_m^{EH+} = \frac{1}{\delta_m} m H^+ J^- \frac{k_\rho^+}{k k_\rho^-} \frac{2i}{\pi a} \tau,$$

$$T_m^{HE+} = k^2 n_-^2 T_m^{EH+},$$

$$T_m^{HH+} = \frac{1}{\delta_m} \frac{k_\rho^+}{k_\rho^-} (n_-^2 \alpha_{J^-H^+} - n_+^2 \alpha_{H^+J^-}) \frac{2i}{\pi a}. \tag{C6}$$

The components of the internal reflection matrix are

$$R_m^{EE-} = \frac{1}{\delta_m}[(\alpha_{J^-H^+} - \alpha_{H^+J^-})(n_-^2 \alpha_{H^-H^+} - n_+^2 \alpha_{H^+H^-}) - m^2 J^- H^- H^{+2} \tau^2],$$

$$R_m^{EH-} = \frac{1}{\delta_m} m H^{+2} \frac{k_\rho^+}{k k_\rho^-} \frac{2i}{\pi a} \tau,$$

$$R_m^{HE-} = k^2 n_-^2 R_m^{EH-},$$

$$R_m^{HH-} = \frac{1}{\delta_m}[(\alpha_{H^-H^+} - \alpha_{H^+H^-})(n_-^2 \alpha_{J^-H^+} - n_+^2 \alpha_{H^+J^-}) - m^2 J^- H^- H^{+2} \tau^2]. \tag{C7}$$

The components of the interior transmission matrix are

$$T_m^{EE-} = \frac{1}{\delta_m} \frac{k_\rho^-}{k_\rho^+} n_+^2 (\alpha_{J^-H^+} - \alpha_{H^+J^-}) \frac{2i}{\pi a},$$

$$T_m^{EH-} = \frac{1}{\delta_m} m H^+ J^- \frac{k_\rho^-}{k k_\rho^+} \frac{2i}{\pi a} \tau,$$

$$T_m^{HE-} = k^2 n_+^2 T_m^{EH-},$$

$$T_m^{HH-} = \frac{1}{\delta_m} \frac{k_\rho^-}{k_\rho^+} (n_-^2 \alpha_{J^-H^+} - n_+^2 \alpha_{H^+J^-}) \frac{2i}{\pi a}. \tag{C8}$$

[1] E. M. Purcell, Phys. Rev. **69**, 681 (1946).
[2] D. Kleppner, Phys. Rev. Lett. **47**, 233 (1981).
[3] R. G. Hulet, E. S. Hilfer, and D. Kleppner, Phys. Rev. Lett. **55**, 2137 (1985).
[4] K. H. Drexhage, J. Lumin. **1–2**, 693 (1970).
[5] E. Snoeks, A. Lagendijk, and A. Polman, Phys. Rev. Lett. **74**, 2459 (1995).
[6] E. Yablonovitch, Phys. Rev. Lett. **58**, 2059 (1987).
[7] S. John, Phys. Rev. Lett. **58**, 2486 (1987).
[8] J. D. Joannopoulos, R. D. Meade, and J. N. Winn, *Photonic Crystals: Molding the Flow of Light* (Princeton University Press, Princeton, NJ, 1995).
[9] *Photonic Band Gap Materials*, edited by C. M. Soukoulis (Kluwer Academic, Dordrecht, 1996).
[10] S. John and J. Wang, Phys. Rev. Lett. **64**, 2418 (1990).
[11] Y. Yang and S-Y. Zhu, Phys. Rev. A **62**, 013805 (2000).
[12] N. Vats, S. John, and K. Busch, Phys. Rev. A **65**, 043808 (2002).
[13] Z-Y. Li and Y. Xia, Phys. Rev. B **63**, 121305 (2001).
[14] S. John and T. Quang, Phys. Rev. A **50**, 1764 (1994).
[15] N. Vats and S. John, Phys. Rev. A **58**, 4168 (1998).
[16] K. Busch, N. Vats, S. John, and B. C. Sanders, Phys. Rev. E **62**, 4251 (2000).
[17] P. Lambropoulos, G. M. Nikolopoulos, T. R. Nielsen, and S.

Bay, Rep. Prog. Phys. **63**, 455 (2000).
[18] M. Florescu and S. John, Phys. Rev. A **64**, 033801 (2001).
[19] X-H. Wang, B-Y. Gu, R. Wang, and H-Q. Xu, Phys. Rev. Lett. **91**, 113904 (2003).
[20] S. John and T. Quang, Phys. Rev. Lett. **78**, 1888 (1997).
[21] S. John and T. Quang, Phys. Rev. Lett. **74**, 3419 (1995).
[22] S. Bay, P. Lambropoulos, and K. Molmer, Phys. Rev. A **57**, 3065 (1998).
[23] S. Bay, P. Lambropoulos, and K. Molmer, Phys. Rev. Lett. **79**, 2654 (1997).
[24] M. Woldeyohannes and S. John, Phys. Rev. A **60**, 5046 (1999).
[25] D. G. Angelakis, E. Paspalakis, and P. L. Knight, Phys. Rev. A **64**, 013801 (2001).
[26] J. Martorell and N. M. Lawandy, Phys. Rev. Lett. **65**, 1877 (1990).
[27] M. Megens, J. E.G.J. Wijnhoven, A. Lagendijk, and W. L. Vos, J. Opt. Soc. Am. B **16**, 1403 (1999).
[28] T. Yamasaki and T. Tsutsui, Appl. Phys. Lett. **72**, 1957 (1998).
[29] E. P. Petrov, V. N. Bogomolov, I. I. Kalosha, and S. V. Gaponenko, Phys. Rev. Lett. **81**, 77 (1998).
[30] S. G. Romanov, T. Maka, C. M. Sotomayor Torres, M. Muller, and R. Zentel, Appl. Phys. Lett. **75**, 1057 (1999).
[31] A. F. Koenderink, L. Bechger, H. P. Schriemer, A. Lagendijk, and W. L. Vos, Phys. Rev. Lett. **88**, 143903 (2002).
[32] R. Sprik, B. A. van Tiggelen, and A. Lagendijk, Europhys. Lett. **35**, 265 (1996).
[33] K. Busch and S. John, Phys. Rev. E **58**, 3896 (1998).
[34] Z-Y. Li, L-L. Lin, and Z-Q. Zhang, Phys. Rev. Lett. **84**, 4341 (2000).
[35] D. P. Fussell, R. C. McPhedran, C. Martijn de Sterke, and A. A. Asatryan, Phys. Rev. E **67**, 045601 (2003).
[36] V. Lousse, J-P. Vigneron, X. Bouju, and J-M. Vigoureux, Phys. Rev. B **64**, 201104 (2001).
[37] A. Moroz, Europhys. Lett. **46**, 419 (1999).
[38] M. Wubs and A. Lagendijk, Phys. Rev. E **65**, 046612 (2002).
[39] Y. Xu, J. S. Vuckovic, R. K. Lee, O. J. Painter, A. Scherer, and A. Yariv, J. Opt. Soc. Am. B **16**, 465 (1999).
[40] J-Ki. Hwang, H-Y. Ryu, and Y-H. Lee, Phys. Rev. B **60**, 4688 (1999).
[41] R. K. Lee, Y. Xu, and A. Yariv, J. Opt. Soc. Am. B **17**, 1438 (2000).
[42] C. Hermann and O. Hess, J. Opt. Soc. Am. B **19**, 3013 (2002).
[43] M. Paulus, P. Gay-Balmaz, and O. J. F. Martin, Phys. Rev. E **62**, 5797 (2000).
[44] O. J. F. Martin, C. Girard, and A. Dereux, Phys. Rev. Lett. **74**, 526 (1995).
[45] T. Sondergaard and B. Tromborg, Phys. Rev. B **66**, 155309 (2002).
[46] A. A. Asatryan, K. Busch, R. C. McPhedran, L. C. Botten, C. Martijn de Sterke, and N. A. Nicorovici, Phys. Rev. E **63**, 046612 (2001); Opt. Express **8**, 191 (2001).
[47] M. Plihal and A. A. Maradudin, Phys. Rev. B **44**, 8565 (1991).
[48] R. D. Meade, K. D. Brommer, A. M. Rappe, and J. D. Joannopoulos, Appl. Phys. Lett. **61**, 495 (1992).
[49] M. Bayindir, E. Cubukcu, I. Bulu, T. Tut, E. Ozbay, and C. M. Soukoulis, Phys. Rev. B **64**, 195113 (2001).
[50] U. Gruning, V. Lehmann, and C. M. Engelhardt, Appl. Phys. Lett. **68**, 747 (1996); J. Schilling, R. B. Wehrspohn, A. Birner, F. Muller, R. Hillebrand, U. Gosele, S. W. Leonard, J. P. Mondia, F. Genereux, H. M. van Driel, P. Kramper, V. Sandoghdar, and K. Busch, J. Opt. A, Pure Appl. Opt. **3**, S121 (2001).
[51] W. M. Robertson, G. Arjavalingam, R. D. Meade, K. D. Brommer, A. M. Rappe, and J. D. Joannopoulos, Phys. Rev. Lett. **68**, 2023 (1992).
[52] A. Rosenberg, R. J. Tonucci, H-B. Lin, and A. J. Campillo, Opt. Lett. **21**, 830 (1996).
[53] J. C. Knight, J. Broeng, T. A. Birks, and P. St. J. Russell, Nature (London) **282**, 1476 (1998).
[54] E. Chow, S. Y. Lin, S. G. Johnson, P. R. Villeneuvre, J. D. Joannopoulos, J. R. Wendt, G. A. Vawter, W. Zubrzycki, H. Hou, and A. Alleman, Nature (London) **407**, 983 (2000).
[55] V. V. Poborchii, T. Tada, and T. Kanayama, Appl. Phys. Lett. **75**, 3276 (1999).
[56] M. V. Kotlyar, T. Karle, M. D. Settle, L. O'Faolain, and T. F. Krauss, Appl. Phys. Lett. **84**, 3588 (2004).
[57] P. L. Phillips, J. C. Knight, B. J. Mangan, P. St. J. Russell, M. D. B. Charlton, and G. J. Parker, J. Appl. Phys. **85**, 6337 (1999).
[58] R. D. Meade, A. Devenyi, J. D. Joannopoulos, O. L. Alerhand, D. A. Smith, and K. Kash, J. Appl. Phys. **75**, 4753 (1994).
[59] A. Mekis, S. Fan, and J. D. Joannopoulos, Phys. Rev. B **58**, 4809 (1998).
[60] P. R. Villeneuve, S. Fan, and J. D. Joannopoulos, Phys. Rev. B **54**, 7837 (1996).
[61] O. Painter, R. K. Lee, A. Scherer, A. Yariv, J. D. O'Brien, P. D. Dapkus, and I. Kim, Science **284**, 181 (1999).
[62] M. Imada, A. Chutinan, S. Noda, and M. Mochizuki, Phys. Rev. B **65**, 195306 (2002).
[63] W. J. Wadsworth, J. C. Knight, W. H. Reeves, and P. St. J. Russell, Electron. Lett. **36**, 1452 (2000).
[64] M. O. Scully and M. Suhail Zubairy, *Quantum Optics* (Cambridge University Press, Cambridge, England, 1997).
[65] R. Loudon, *The Quantum Theory of Light* (Oxford University Press, New York, 1983).
[66] B. Balian and C. Bloch, Ann. Phys. (N.Y.) **64**, 271 (1971).
[67] P. Sheng, *Introduction to Wave Scattering, Localization, and Mesoscopic Phenomena* (Academic Press, London, 1995).
[68] O. J. Martin and N. B. Piller, Phys. Rev. E **58**, 3909 (1998).
[69] W. C. Chew, *Waves and Fields in Inhomogeneous Media* (IEEE Press, New York, 1995).
[70] G. Nienhuis and C. Th. J. Alkemade, Physica C **81**, 181 (1976).
[71] P. M. Morse and H. Feshbach, *Methods in Theoretical Physics* (McGraw-Hill, New York, 1953).
[72] C-T Tai, *Dyadic Green Functions in Electromagnetic Theory* (IEEE Press, New York, 1994).
[73] T. P. White, B. T. Kuhlmey, R. C. McPhedran, D. Maystre, G. Renversez, C. Martijn de Sterke, and L. C. Botten, J. Opt. Soc. Am. B **19**, 2322 (2002).
[74] M. Abramowitz and I. A. Stegun, *Handbook of Mathematical Functions* (Dover, New York, 1972).
[75] C. G. Poulton, R. C. McPhedran, N. A. Nicorovici, L. C. Botten, and A. B. Movchan, *Asymptotics of Photonic Band Structures for Doubly-Periodic Arrays, IUTAM Symposium on Mechanical and Electromagnetic Waves in Structured Media* (Kluwer Academic Publishers, Boston, 2001).
[76] B. T. Kuhlmey, T. P. White, G. Renversez, D. Maystre, L. C. Botten, C. Martijn de Sterke, and R. C. McPhedran, J. Opt. Soc. Am. B **19**, 2331 (2002).

[77] A. W. Snyder and J. D. Love, *Optical Waveguide Theory* (Chapman and Hall, London, 1983).
[78] Y. Fink, J. N. Winn, S. Fan, C. Chen, J. Michel, J. D. Joannopoulos, and E. L. Thomas, Science **282**, 1679 (1998).
[79] S. D. Hart, G. R. Maskaly, B. Temelkuran, P. H. Prideaux, J. D. Joannopoulos, and Y. Fink, Science **296**, 510 (2002).
[80] L. Rogobete, H. Schniepp, V. Sandoghdar, and C. Henkel, Opt. Lett. **28**, 1736 (2003).
[81] *Properties, Processing and Application of Glass and Rare Earth-Doped Glasses for Optical Fibres*, edited by D. Hewak (IEE, Stevenage, 1998), Parts B, C, and D.
[82] J. Wang, M. S. Gudiksen, X. Duan, Y. Cui, and C. M. Lieber, Science **293**, 1455 (2001).